machines

MDPI

Article

Effect of the Computational Model and Mesh Strategy on the Springback Prediction of the Sandwich Material

Pavel Solfronk *, Jiří Sobotka and David Koreček

Department of Engineering Technology, Faculty of Mechanical Engineering, Technical University of Liberec, Studentska 1402/2, 46117 Liberec, Czech Republic; jiri.sobotka@tul.cz (J.S.); david.korecek@tul.cz (D.K.)
* Correspondence: pavel.solfronk@tul.cz; Tel.: +420-485-353-374

Abstract: The effect of the computational model and mesh strategy on the springback prediction of the thin sandwich material made of micro-alloyed steel was investigated in this paper. To verify the chosen computational strategy, a comparison of the experimentally obtained specimen (U-bending) with the FEA result was performed. The Vegter yield criterion combined both with the isotropic and kinematic hardening law was used for the calculation. In addition, the effect of the deformation mesh element (surface and volume) on the accuracy of the springback prediction was investigated. It was concluded that the choice of the volume deformation mesh does not significantly improve the accuracy of the results. Moreover, it is quite a time-consuming approach. The much greater influence was monitored by concerning the selection of hardening law, where the anisotropic one was more suitable to be used on the springback prediction of a given sandwich material.

Keywords: sandwich; springback; Vegter yield criterion; numerical simulation; PAM-STAMP 2G; isotropic hardening law; kinematic hardening law; bending; Bauschinger effect

check for updates

Citation: Solfronk, P.; Sobotka, J.; Koreček, D. Effect of the Computational Model and Mesh Strategy on the Springback Prediction of the Sandwich Material. *Machines* **2022**, *10*, 114. https://doi.org/10.3390/machines10020114

Academic Editors: Marek Kočiško and Martin Pollák

Received: 27 December 2021
Accepted: 2 February 2022
Published: 3 February 2022

Publisher's Note: MDPI stays neutral with regard to jurisdictional claims in published maps and institutional affiliations.

1. Introduction

In recent years, there has been a steady development in the range of materials ready to be used in various areas of industry. Such materials include, for example, so-called sandwich materials, which derive benefits from the advantageous utility properties of different material groups (e.g., combination metal-plastic). Nowadays, sandwich materials are mainly used either to reduce the overall weight of given products or due to their specific properties to reduce noise or vibrations.

The increasingly widespread utilisation of various types of sandwich materials, not only in the automotive industry, naturally also brings with it the necessity to know their specific deformation behaviour (generally material characteristics) under various loading conditions. For this reason, sandwich materials have been subjected to continuous testing and determination of their deformation behaviour, e.g., Fischer [1] performed static and dynamic tests (compression, shear, bending and impact tests) of aluminium foldcore specimens and compared the results with the finite element analysis (FEA). The effect of variable mechanical properties of the sandwich beam core in light of elastic loading was investigated by Grygorowicz et al. [2]. Moreover, other authors focused, for example, on the hardness measurement and thermal analysis of aluminium-based sandwich composites [3], mechanical, fatigue and thermal properties of the honeycomb sandwich structures [4–12] or properties of sandwich materials when joining technologies are taken into account. For example, Gladkovsky [13] researched a feature of interface structure at explosive welding and Nilsson [14] tested the fatigue properties of laser stake-welds. Generally, the joining of sandwich materials represents very important research and was investigated by many authors such as, e.g., [15–17]. Nevertheless, before the application of sandwich material, it is very important not only to verify these results but also to incorporate the chosen material and its material behaviour into the whole production process. For this reason, numerical

simulations are very often used during the pre-production phase. A general overview of the numerical simulation used in the sheet metal forming is quite clearly described, e.g., by Ablat [18].

Numerical simulations are nowadays commonly used to verify the material properties as well as the deformation behaviour of materials chosen for the production of a given component. Mostly a finite element method is used. These analyses (FEA) then provide very important knowledge about the behaviour of the material during the actual manufacturing process, without the need for real tools, machines and materials.

One of the most important phenomena that affects the dimensional accuracy of given products within the metal forming technologies is so-called springback, which is elastically driven and thus represents the change of the final shape after unloading. There are different methods of how to eliminate the springback (e.g., modification of tool or trial and error method), but it is always preferable to predict the springback magnitude.

In light of the springback prediction, two basic approaches can be generally used. The first is an analytical model and the other one rests in the application of a finite element analysis (FEA). Analytical (or semi-analytical) modelling of springback can be found, e.g., in [19–28]. The greatest disadvantage of such an approach rests in the utilisation of some simplifications, so their accuracy is generally not so high compared to the results of FEA.

On the other hand, the proper use of FEA is largely dependent on the accuracy of its own input data (generally input parameters), which is especially important from the springback prediction point of view. Han et al. [29] considered the input parameters in springback simulation and determined the best combination of such input parameters. Mertin et al. [30] determined the elastoplastic material parameters of HSS by using the inverse modelling approach. Trzepieciński used a genetic algorithm to optimise the number of input parameters of the multilayer perceptron. It was found that the most important variable affecting the springback coefficient is the punch bend depth. Gu [31] increased the accuracy of springback prediction by the use of cyclic sheet metal test methods such as uniaxial tensile-compression and cyclic shear tests. Li [32] investigated the influence of process parameters (e.g., friction and clearance) on the springback at the free bending process. Seo [33] evaluated the effect of constitutive equations on the springback prediction accuracy. It was concluded that it is always very important to use appropriate constitutive equations. Liu et al. [34] found that springback prediction in cold roll forming is significantly improved by incorporating the Young's modulus variation into the FEA simulations.

In addition to these two basic approaches, the use of so-called artificial neutral networks (ANN) in the material science has become more widespread in recent years, e.g., Pouraliakbar [35] developed an ANN model to predict the toughness of HSLA steel. Nowadays, in light of springback prediction, utilisation of ANN represents an alternative tool for springback prediction, especially regarding that in light of nonlinear recovery, FEM has become quite complicated to achieve reliable results as it is concluded, e.g., by [36]. However, it is still a developing procedure, so, e.g., Angsuseranee [37] compared the efficiency of springback and sidewall curl prediction of AHSS in the U-bending process by the FEM and ANN and it was found that FEM was more efficient than the ANN approach. On the other hand, Miranda [38] combined the use of ANN and learning toll with a simulation and data generation tool to conclude that such a methodology can model the complex nonlinear behaviour with sufficient reliability.

Utilisation and development of the different material constitutive models is quite digestedly presented in the work of Zhu et al. [39], where the effect of variable elastic modulus, nonlinear recovery, the isotropic hardening model and hardening model taking into account the Bauschinger effect are summarised. Quite a lot of different yield criterions are mentioned in this paper (e.g., Hill48, Barlat89, Barlat2003, BBC 2005, etc.) [39]. However, the Vegter yield criterion is missing in this case. The effect of the variations in the elastic modulus and its influence on the springback prediction is, e.g., studied by Chatti et al. [40], where a new model to take into account variation in the elastic modulus was proposed. Jung [41] developed an elastoplastic material constitutive model to take into account already

the effect of anisotropy change at loading and springback recovery for AHSS materials. A combined isotropic–kinematic hardening model was modified in this case having a good matching with the real samples. Baara et al. [42] improved the accuracy of the finite element software (Abaqus) by introducing the new constitutive hardening model that can predict the final shape of a part that changes its dimensions after forming. The modification of the original Chord model and its combination with nonlinear isotropic–kinematic revealed a higher accuracy of this new model.

However, in light of the springback prediction, it is always important to consider the mutual effect between all major input parameters (elastic modulus, geometry, yield criterion and hardening laws). That is why quite a lot of papers deal with the effect of these parameters on the springback prediction. Mulidrán et al. [43,44] combined different yield criterions and hardening laws to determine the accuracy of springback prediction, in these cases for DP steel and aluminium alloy AA6451, respectively. Trzepiecinski and Lemu [45] studied the springback behaviour of steel DC04 under the different input parameters (geometry, conditions and material) for FEA (here, Abaqus). The work of Naofal et al. [46] presented calibrated plasticity models arising from the appropriate tests to predict springback during the roll forming process. In this case, the Yoshida-Uemori hardening law revealed a higher accuracy to predict springback than the isotropic hardening law. Sumikawa [47] developed and implemented an FEM software material model, which takes into account not only average Young´s modulus and Bauschinger effect, but also elastic and plastic anisotropy. It was concluded that besides the Bauschinger effect and Young´s modulus, there is also a great effect arising from elastic and plastic anisotropy on the results of springback predictions. The effects of the different yield criterions (Hill48 and Hill90), bending radii and directions on the aluminium alloys springback are described by Slota et al. [48].

In this paper, the springback prediction of the sandwich material was performed by using the FEA. Due to the previous results (see above), only the Vegter yield criterion was used and was combined with the two hardening laws (isotropic and kinematic). In addition to that, the effect of mesh strategy (selection of surface or volume elements) on the springback prediction accuracy was investigated as well. This quite complex combination (sandwich material–two hardening laws–type of mesh elements) of input parameters can be considered as the greatest novelty of this paper.

2. Materials and Methods

For the tests, the sandwich material CR270Y340T-LA -EG47/47-E-R-O (designation according to the standard VW 50065) was chosen. It is a micro-alloyed, electro-galvanized sheet designed for the production of car-body outer panels. Concerning the increased requirements for acoustic vibration absorption, this tested material was supplied as a sandwich with a layer of thickness as follows: 0.4–0.1–0.4 mm. The core material was identified by using the Fourier transform infrared spectroscopy (FTIR) on a device Nicolet iS10 manufactured by the company Thermo Scientific (Waltham, MA, USA). The method is based on the absorption of infrared radiation as it passes through the specimen, during which changes in the rotational and vibrational energy levels of the molecule occur as a function of the molecular dipole moment changes. The resulting infrared spectrum is a functional dependence of the energy, usually expressed in percent of transmittance or absorbance units, on the wavelength of incident radiation. For the present analysis, the attenuated total reflection (ATR) technique was used and the measured spectra of the individual materials (32 scans were used) were compared with the spectra in the instrument's database. From the results of the IR spectrometry, it could be concluded that it was an acrylate copolymer. The identification of core material was carried out for further material testing of the sandwich core mechanical properties.

The chemical composition analysis was performed on a Bruker-Quantron spark-optical emission spectrometer Q4 Tasman. Such an analysis was determined based on 5 measurements. The results of the chemical composition analysis are given in Table 1.

Table 1. Chemical composition of the tested sandwich material.

Chemical Element	C	Si	Mn	Al	P	S	Ti	Nb
Composition [wt%]	0.097	0.406	0.746	0.211	0.016	0.013	0.122	0.074

The subsequent structural analysis was carried out on a TESCAN MIRA 3 electron scanning microscope. From the results it is clear that the structure was a ferritic one with the dispersed particles containing an increased content of Mn, Si and Al micro-alloys. The analysed structure can be seen in Figure 1 (left) and detail of the particle is shown in Figure 2 (right). Finally, the EDX bulk analysis arising from the analysed structure is given in Figure 2.

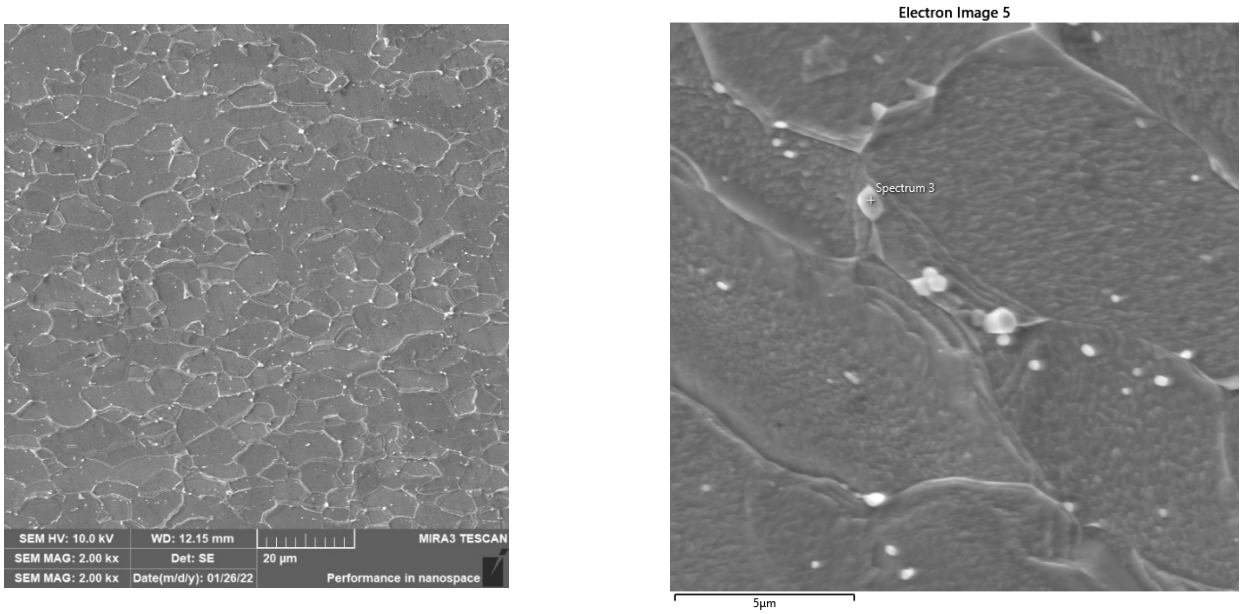

Figure 1. Structure of the tested sandwich material (**left**) and detail of the particle (**right**).

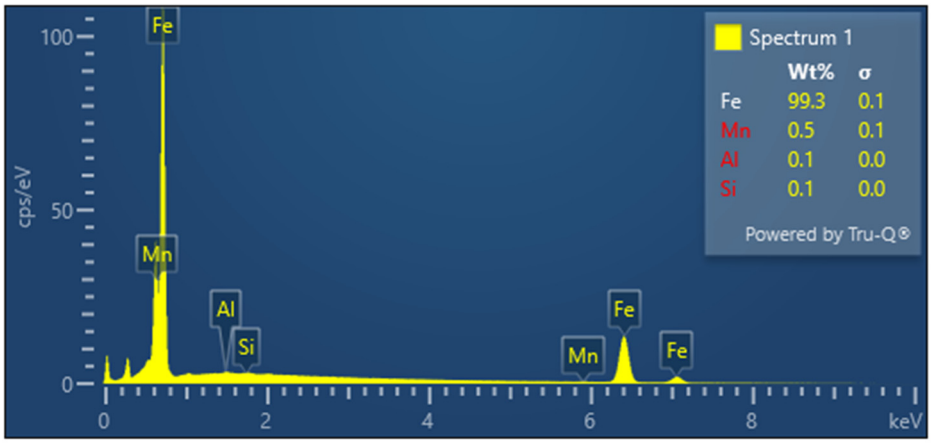

Figure 2. EDX bulk analysis.

2.1. Static Tensile Test

A static tensile test was used to determine the basic material characteristics of the tested material. With a view to the future use of the experimentally obtained data for the definition of the material model in numerical simulations, these tests were already performed for specimens taken in the directions 0°, 45° and 90° concerning the rolling direction. In order to eliminate any material anomalies, material characteristic values were

determined each time from a set of 5 measured specimens. The shape and dimensions of the test specimens were chosen in accordance with the standard EN ISO 6892-1. In addition, the methodology of test execution and evaluation was in accordance with the standard above-mentioned EN ISO 6892-1. The static tensile test was carried out on a modernized device TIRA test 2300 using the software Labtest v.4 to evaluate all basic mechanical properties of the tested material (proof yield strength $R_{p0.2}$, ultimate strength R_m, total ductility A_{80mm}, uniform ductility A_g and Young´s modulus E). The plastic strain ratio (Lankford parameter) r was determined in accordance with the standard ISO 10113 in the interval of true plastic strain values from 10% to 20%. The results of the individual material quantities are summarised in Table 2. Engineering stress R (MPa) vs. engineering strain ε (1), thus so-called engineering stress–strain curves (regarding the individual rolling directions) are shown in Figure 3. The evaluation of the mechanical values given in Table 2 was carried out by considering the measured force values to the whole cross-section, i.e., the measured values represent the average values of mechanical properties for the three layers of the tested sandwich material (steel-plastic-steel).

Table 2. Basic material properties of the tested sandwich material.

Direction	$R_{p0.2}$ (MPa)	R_m (MPa)	A_g (%)	A_{80mm} (%)	$r_{10–20}$ (1)	E (MPa)
0°	291.7	426.5	17.8	23.1	1.335	174,283
45°	299.6	418.3	18.9	27.1	1.515	183,718
90°	307.7	428.5	18.1	26.6	1.622	179,928

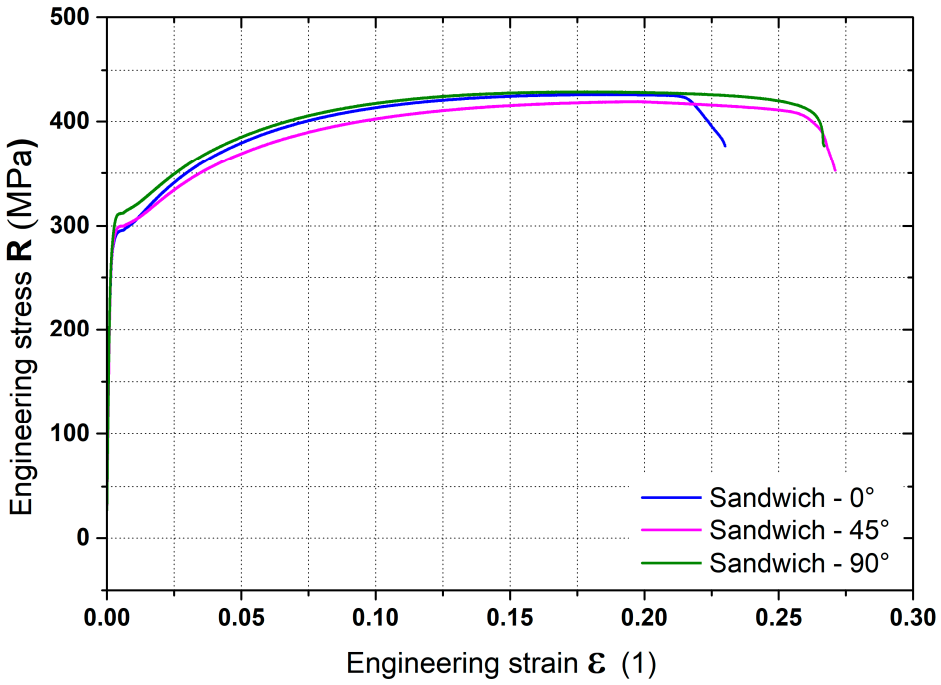

Figure 3. Engineering stress–strain curves (static tensile test) of tested sandwich material.

A numerical simulation has to be a stress–strain curve (hardening curve) entered as a dependence of true stress (effective stress) vs. true plastic strain. Measured dependences of the true stress vs. true plastic strain for the individual rolling directions 0°, 45° and 90° were subsequently approximated (fitted) using the Krupkowski law (power-law function) according to Equation (1).

$$\sigma = K\,(\varepsilon_{pl} + \varepsilon_0)^n \quad (1)$$

where:

σ—true stress (effective stress) (MPa)
K—strength coefficient (MPa)
ε_{pl}—true plastic strain (1)
ε_0—offset true strain (pre-strain) (1)
n—strain hardening exponent (1)

An approximation of the stress–strain curve (hardening curve) was performed within the interval from 1% up to A_g in the software OriginPro 9.0. The advantage of defining the hardening curve by using the Krupkowski hardening law is the simple possibility of integrating this function and thus it is easy to express the equivalent plastic work parametrically in dependence on the true strain and the approximation constants arising from such a function. An example of the approximation result can be seen in Figure 4. The results of the obtained approximation constants are presented in Table 3.

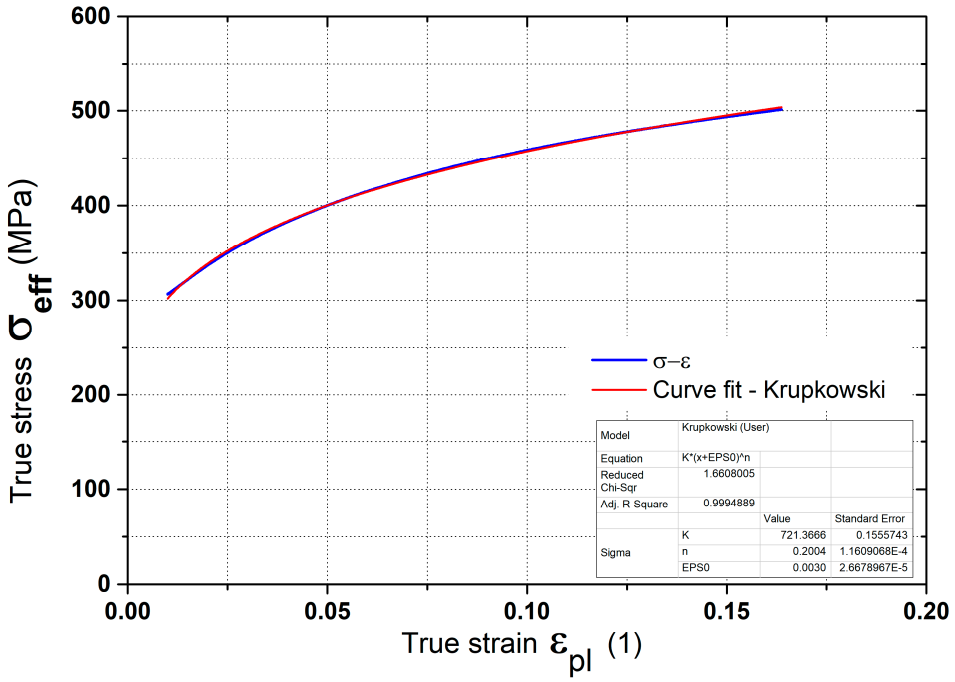

Figure 4. True stress–strain curve (STT) and application of the Krupkowski law.

Table 3. Stress–strain curve approximation constants from the static tensile test.

Direction	K (MPa)	n (1)	ε_0 (1)
0°	720.6	0.1995	0.0030
45°	707.6	0.2025	0.0065
90°	726.9	0.2039	0.0067

2.2. Hydraulic Bulge Test

When testing material by static tensile testing, the test specimen was deformed only by the uniaxial tension (uniaxial tensile stress state). To obtain information about the material deformation behaviour under the multi-axial loading, a hydraulic bulge test (HBT) was mostly performed. The principle of this test rests in stretching the specimen into the circular die by applying the pressure of fluid until a crack occurs. Similar to the static tensile test, the dependence of the true stress vs. true plastic strain (again true stress–strain curve) is evaluated. Figure 5 shows an element of the test specimen together with the parameters used to derive the stress in the test specimen during the HBT.

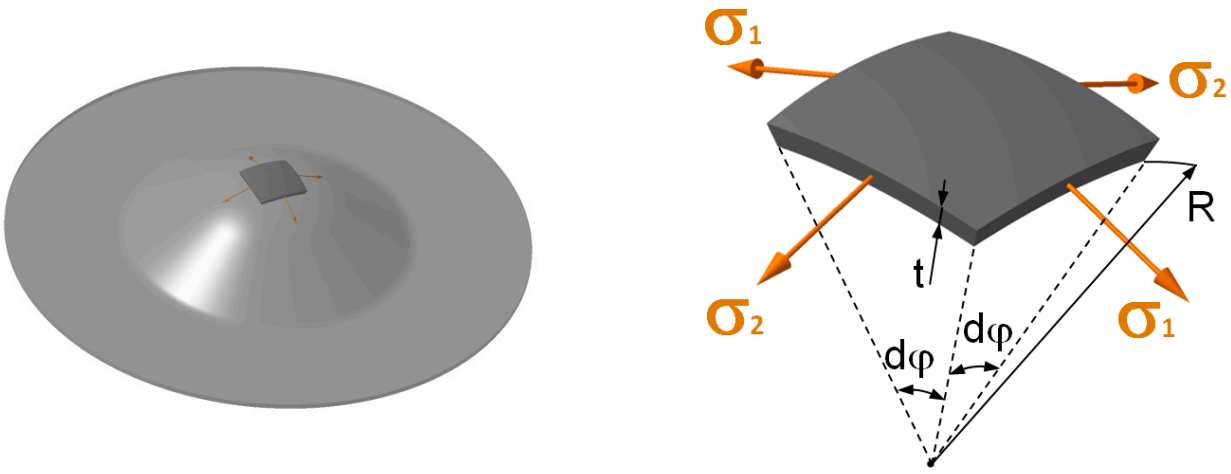

Figure 5. Principle and stress state of the hydraulic bulge test (HBT).

Based on the right part of Figure 5, where the effects of fluid pressure on the specimen element are shown (equilibrium equation), can be acc. to membrane theory derived Equation (2) for the stress in the test specimen wall and so the effective stress σ_{eff} (arising from the Tresca's plastic flow criterion) can be finally expressed by relation (3).

$$\sigma_{HBT} = \frac{p \cdot R}{2 \cdot t} \tag{2}$$

$$\sigma_{eff} = \frac{p \cdot R}{2 \cdot t} + \frac{p}{2} \tag{3}$$

where:

p—hydraulic pressure (MPa)
R—radius of curvature (mm)
t—actual thickness of specimen (mm)

Finally, effective strain ε_{eff} can be calculated using principal strains $\varepsilon_{1,2,3}$ according to Equation (4)

$$\varepsilon_{eff} = \frac{\sqrt{2}}{3} \cdot \sqrt{(\varepsilon_1 - \varepsilon_2)^2 + (\varepsilon_2 - \varepsilon_3)^2 + (\varepsilon_3 - \varepsilon_1)^2} \tag{4}$$

where:

$\varepsilon_{1,2,3}$—principal strains (1)

Actual thickness of the specimen can be subsequently determined through the principal strain ε_3 (sometimes termed also as a thickness reduction) firstly via the constant volume law (5) and subsequently using Equation (6).

$$\varepsilon_1 + \varepsilon_2 + \varepsilon_3 = 0 \tag{5}$$

$$\varepsilon_3 = \ln\left(\frac{t}{t_0}\right) \tag{6}$$

where:

t—actual thickness (mm)
t_0—initial thickness (mm)

To determine the hardening curve in the HBT, it is therefore necessary to measure the dependence of the test specimen deformation on the hydraulic pressure. That is why a contactless photogrammetry method using the software Mercury RT from the company Sobriety, Ltd. (Kuřim, Czech Republic) was used to measure the true strain values. A scheme of the measurement layout is shown in Figure 6.

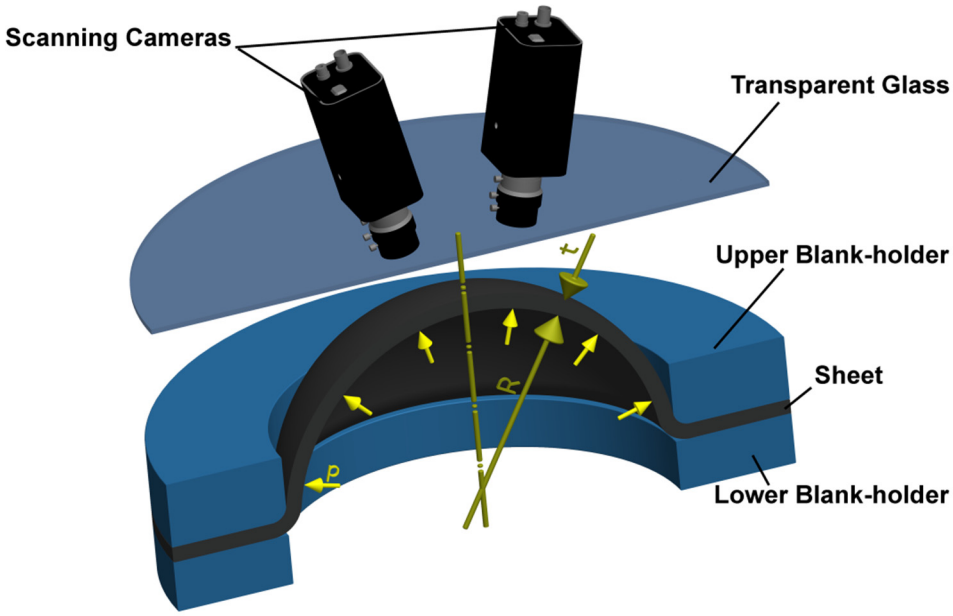

Figure 6. Scheme of the measurement of true stress–strain curve at HBT.

Because stress relaxation occurs when the specimen is loaded, the pressure of the fluid was not increased continuously, but gradually at intervals of 5 s. The value of the pressure increase (pressure step) was chosen to be 0.25 MPa and the own magnitude of the required pressure was controlled by a precision hydraulic servo valve with PID control.

The achievable accuracy of the required pressure was 0.002 MPa. The system of hydraulic pressure activation and its control was solved by a separate hydraulic unit working independently of the hydraulic circuit of the given press.

From the contactless deformation analysis using the system Mercury RT, the magnitudes of major and minor strain (ε_1, ε_2), as well as the radius of curvature R must be detected to subsequently determine the stress–strain curve. For this purpose, two surfaces have been defined on the measured area, in which the system calculates the desired quantities. An example of the analysis area is shown in Figure 7. The larger analysis area (area A) is used to find the radius of curvature R and the smaller area (area B) is used to calculate the major and minor strain, from which the actual thickness of the material can be calculated using Equations (5) and (6). An example of true strain distribution in the relevant area and evolution of the radius of curvature R is shown in Figure 8.

Similar to the static tensile test, a hardening curve was obtained from the measured data, which was then approximated by the Krupkowski law (1). An example of this approximation of the hardening curve from HBT, so under the equi-biaxial stress state, can be seen in Figure 9. The average values of approximation constants obtained under equi-biaxial loading can be seen in Table 4.

Table 4. Stress–strain curve approximation constants from the hydraulic bulge test.

Material	K (MPa)	n (1)	ε_0 (1)
Sandwich	865.1	0.267	0.0076

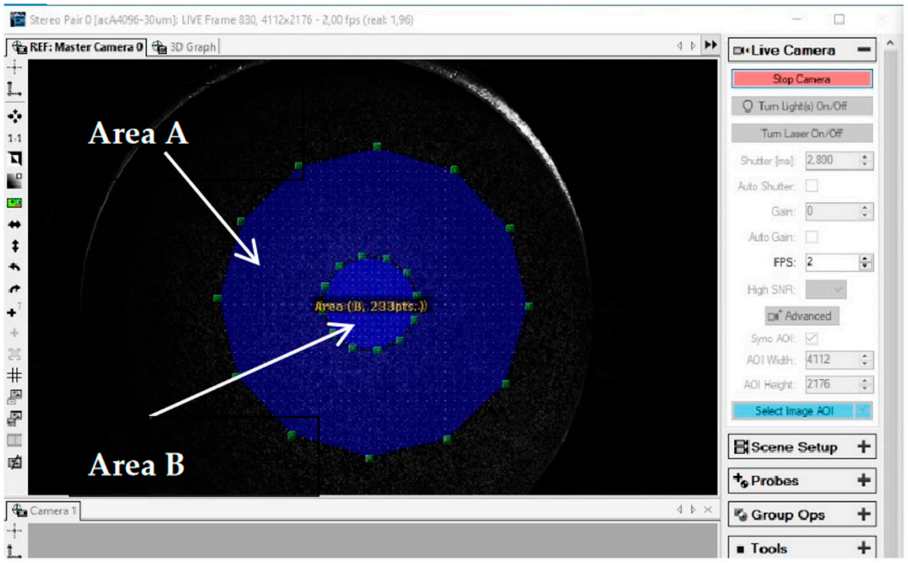

Figure 7. Definition of the analysis areas A and B (software Mercury RT).

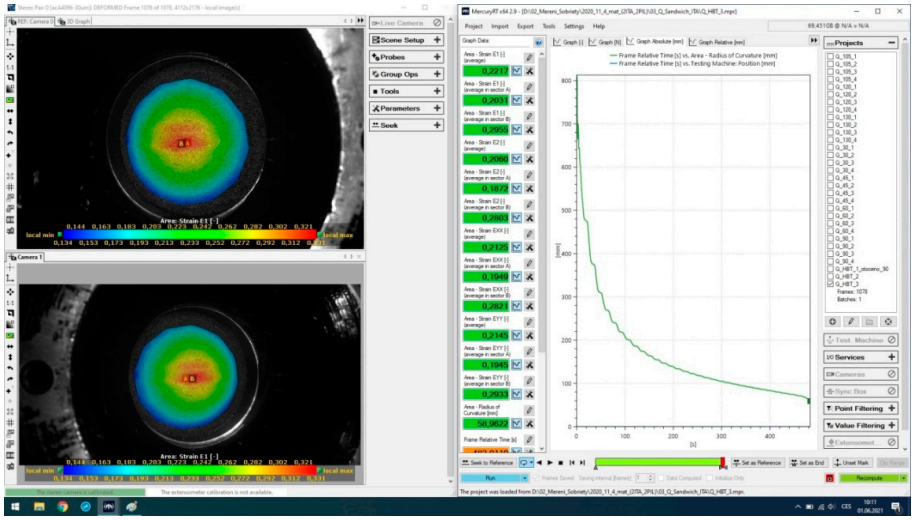

Figure 8. True strain distribution (here ε_1) and evolution of the radius of curvature R.

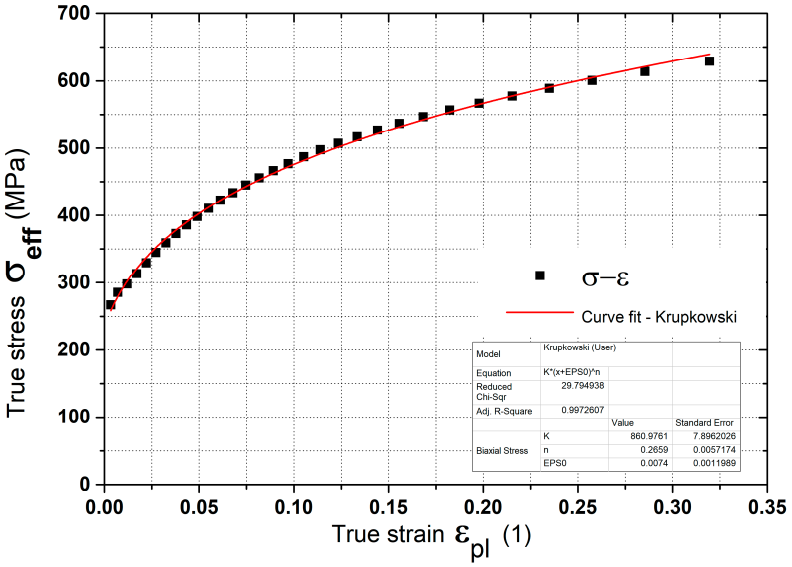

Figure 9. True stress–strain curve from HBT and application of the Krupkowski law.

2.3. Cyclic Test

In addition to the previous tests, we also carried out a cyclic test, which takes the effect of the change of loading direction (+, −), to define the material model termed as Yoshida-Uemori. Due to the compressive stress states, a performance of this test for sheet samples was quite demanding and there was a loss of stability resulting in sample buckling. Thus, a testing jig was proposed as an additional jig for the clamping grips. The testing jig consists of four subdivided supporting grips, which are hydraulically controlled and can prevent the specimen from buckling during the compression. The offset of measured curves from monitored cycles rests in the magnitude of the Bauschinger effect for the tested material. A total of 5 measurements were made under the data scanning frequency of 50 Hz, from which an average curve was determined. The layout of the cyclic test is shown in Figure 10 (left) and results are given in Figure 10 (right).

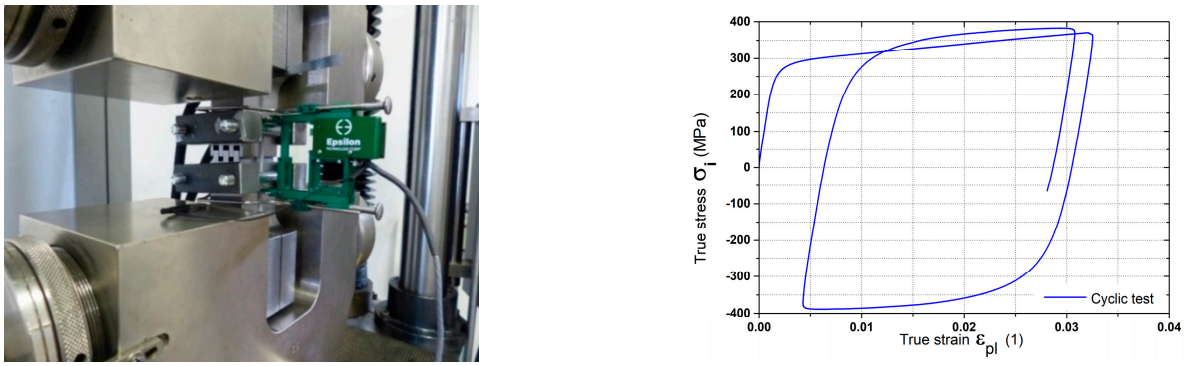

Figure 10. Layout of the cyclic test (**left**) and results of the cyclic test for tested sandwich material (**right**).

2.4. U-Bending of the Specimens

For the experimental determination of the springback, it was suitable to choose such a test when a change of the stress state occurred in the bending area because this case can be fully developed the Bauschinger effect. Concerning the equipment of our laboratory, the U-bending of the workpiece (blank) in the tool with a fixed blank-holder was chosen for the springback analysis. This experiment simulates the process that occurs in a tool at the deep-drawing (stamping) process. During the test, the workpiece is two times bent in the opposite bending direction. The principle of the test is evident from Figure 11, where the scheme of this U-bending test is shown. The test conditions were as follows: distance between fixed blank-holder and die was 0.9 mm (i.e., draw clearance between tool and workpiece was 0 mm). The specimen was in contact with the blank-holder, but there was not force acting at the beginning of the test. The tool is equipped with a lower blank-holder that applies force against the bending punch and prevents the deflection of the sheet. The blank-holder force was developed by a coil spring with an initial force of 4 kN at the start of bending and 6 kN at the end of bending in the bottom dead centre of the bending punch. The die drawing radius was R5, punch drawing radius was R2.5, workpiece dimensions (rectangular shape) 30 mm × 140 mm, bending direction was perpendicular to the rolling direction and own bending was performed on the eccentric press LENP 40.

After finishing the bending test, a specimen was measured by the dimensional and shape analysis on the 3D coordinate measuring device SOMET XZY 464 by the relevant software TANGO1! 3D for own evaluation. As a result of the experimental measurement, there were coordinates of 100 points in *.stp format, which represented the actual shape of the specimen. The principle of measuring the resulting shape is shown in Figure 12.

Software CATIA V5 was used for further processing of the measured points. Through the measured points a curve (spline) was fitted, from which a 30 mm wide area was subsequently extruded. This area had to be further offset by 1.45 mm. This offset value (1.45 mm) was determined by the diameter of the measuring tip (2 mm) and the material thickness

(0.9 mm). The offset plane then represented the midplane of the experimentally measured shape of the specimen. The procedure of obtaining the final shape of the experimental specimen in the Catia environment can be seen in Figure 13. The measured shape of the bent blank was subsequently used as a comparative criterion to verify the match between results of the real experiment and numerical simulation (in this case, software PAM-STAMP 2G was used).

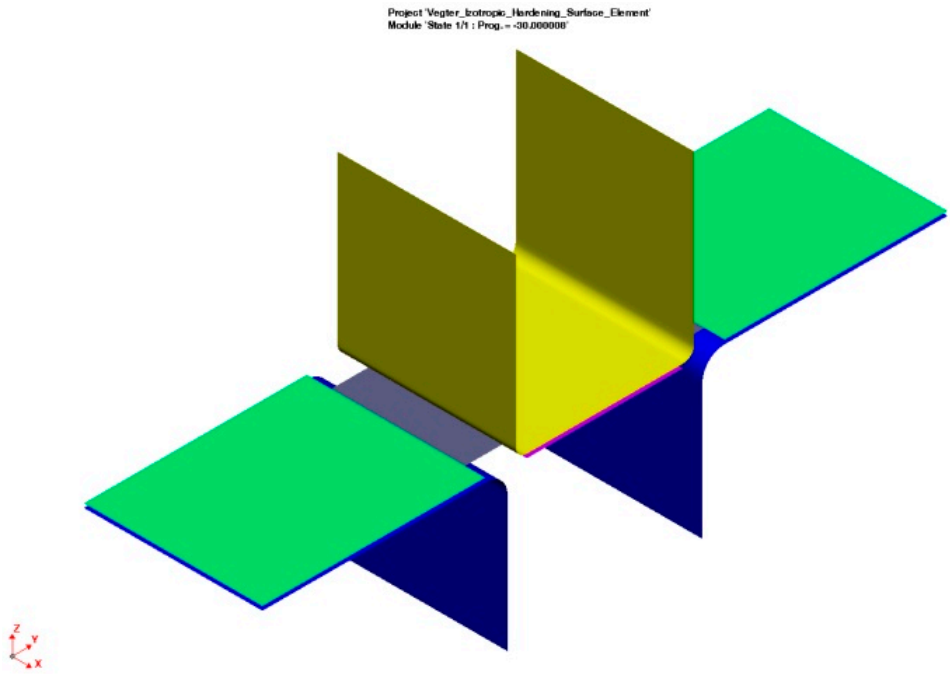

Figure 11. Scheme of the used U-bending experiment.

Figure 12. Determination of the specimen actual shape (device SOMET XZY 464).

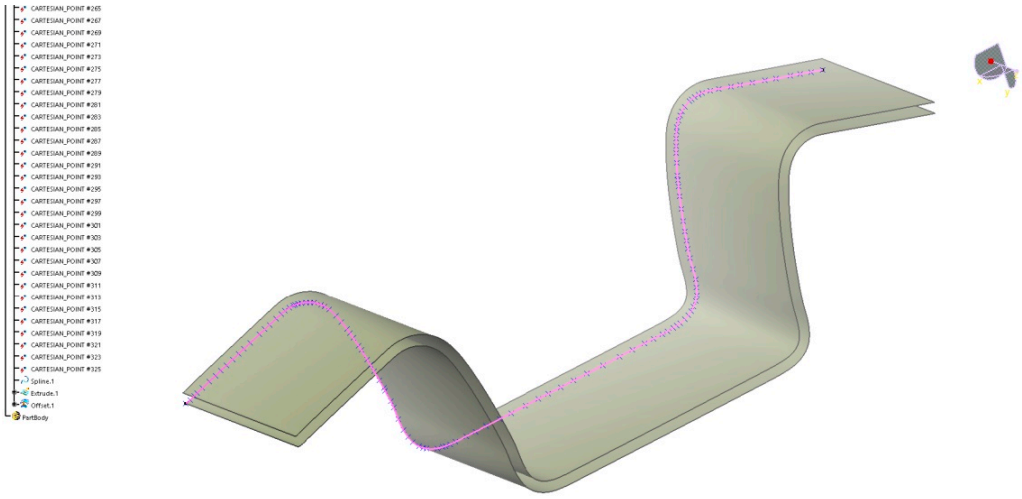

Figure 13. Detection of the experimentally prepared specimen shape (CATIA V5).

3. Numerical Simulation

3.1. Vegter Yield Criterion

The formulation of the Vegter yield criterion (function) is based on the principle of incorporating and using more experimentally measurable data in the definition of this yield criterion. This criterion is established for the general directions of the principal stresses, which do not need to be identical with the direction of sheet anisotropy. Using the suitable orientation of the coordinate system (principal axes), the shear stress components vanish and the stress state in the given zone is defined by using only the normal stress components (thus principal stresses) σ_1 and σ_2. The angle θ denotes the relative rotation between the principal stresses and chosen coordinate system. The principle of the element planar loading and the individual stress components can be subsequently expressed by Equations (7) and (8).

$$\sigma_1 = \frac{\sigma_{xx} + \sigma_{yy}}{2} + \sqrt{\left(\frac{\sigma_{xx} - \sigma_{yy}}{2}\right)^2 + \sigma_{xy}^2} \tag{7}$$

$$\sigma_2 = \frac{\sigma_{xx} + \sigma_{yy}}{2} - \sqrt{\left(\frac{\sigma_{xx} - \sigma_{yy}}{2}\right)^2 + \sigma_{xy}^2} \tag{8}$$

The quadratic Bezier curve is used to mathematically describe the Vegter yield criterion passing through the experimentally determined reference points, as shown in Figure 14. This parametrically determined curve allows the construction of a smooth yield surface with smooth transitions at the reference points (via tangents intersecting in the hinge-points).

Points A and C are experimentally determined reference points defining the yield surface. The tangents to the Bezier curve passing through these reference points are defined by the strain vectors. The intersection of these tangents determines the final shape of the Bezier curve, and it is called a hinge-point [49]. Although the curve does not pass through this hinge-point, its shape strongly depends on this point. Coordinates of any point on the Bezier curve are given by the so-called Bezier parameter μ and position of the hinge-point B (strain vectors). Figure 15 shows part of the curve defining the yield criterion, where coordinates of the point BI denote the yield strength at the equi-biaxial stress state. The position of the point UN denotes the transition between the elastic and plastic state (yield strength) under the uniaxial loading (uniaxial tensile test), and finally point PS defines the yield strength under the plane strain test (so-called plain strain point). Points a and b are the intersections of the tangent line passing through point PS with the tangent line passing through UN and BI, respectively. By introducing an extra input parameter α, which should have a value between 0 and 1, the position of the point PS can be determined (see Figure 15).

However, it is quite difficult to determine the position of the point PS experimentally and for this reason the value $\alpha_{PS} = 0.5$ is very often assumed when defining the yield criterion. A similar problem is arising during the experimental determination of the point SH position characterising the pure shear stress. In this case, the presumption about the symmetry of yield criterion and parameter α_{SH} having the value equal to 0.5 is used, as in the case of plane strain point. In the case of experimental determination of these points, no estimation of such extra input parameter α is necessary and the Vegter yield surface directly passes through these experimentally detected points.

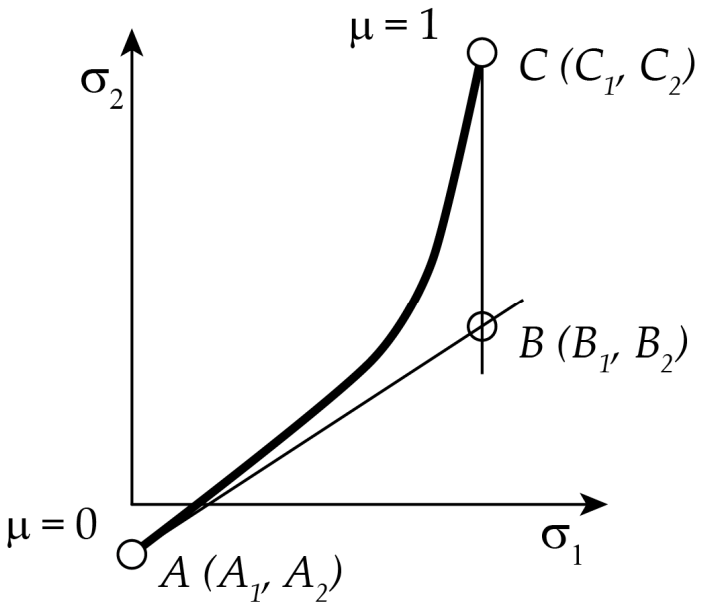

Figure 14. Bezier curve passing through reference points *A* and *C*.

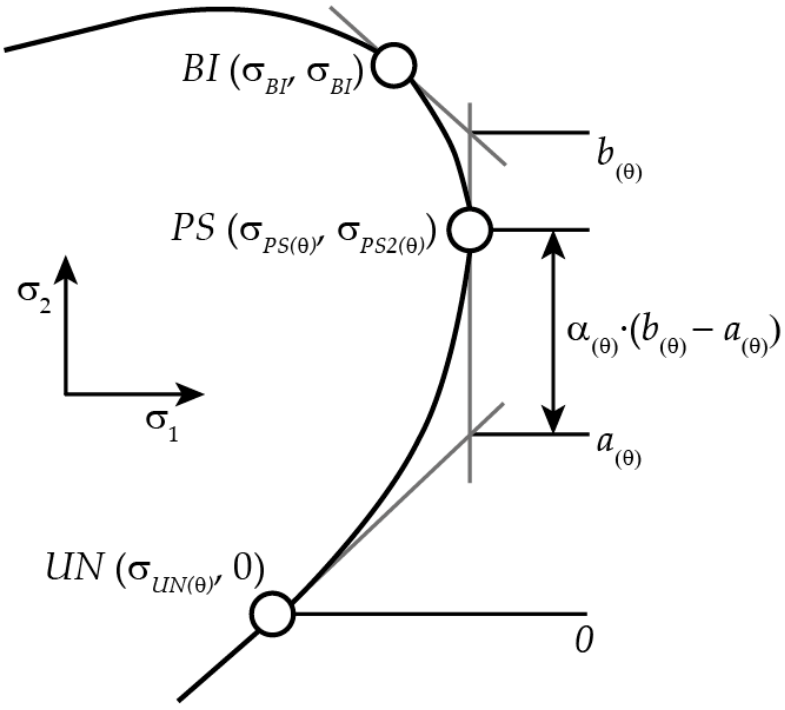

Figure 15. Definition of the plane strain point PS via extra input parameter α [50].

Using the Bezier curve to define the yield criterion, the functional relation can be subsequently expressed by the Equation (9):

$$\varphi + \sigma_f = \frac{\sigma_i}{f_i(\mu, c)} \tag{9}$$

where:

$$f_i(\mu, c) = A_i(c) + 2\mu \cdot (B_i(c) - A_i(c)) + \mu^2 \cdot (A_i(c) + C_i(c) - 2B_i(c)) \tag{10}$$

$$c = cos(2\theta) \tag{11}$$

μ = Bezier parameter ($0 \leq \mu \leq 1$)

A, B, C, are vectors formulating in a two-dimensional stress plane σ_1 and σ_2 the plane stress state condition ($\sigma_3 = 0$). The yield criterion is completely dependent on the three parameters mentioned above but is not uniquely determined due to the interdependence of the parabolic functions. The yield surface is described as the individual parts of the Bezier curve affected by the hinge-point B and passing through the reference points A and C. The total yield surface is constructed through the four quadrants expressing the different stress states. Continuity of the first derivative is required between any part of the yield function. The strain vector is derived as follows:

$$d\varepsilon_{ij} = d\lambda \frac{\partial \varphi}{\partial \sigma_{ij}} \tag{12}$$

$$\frac{\partial \varphi(\sigma_1, \sigma_2, \theta)}{\partial \sigma_{ij}} = \frac{\partial \varphi}{\partial \sigma_1} \cdot \frac{\partial \sigma_1}{\partial \sigma_{ij}} + \frac{\partial \varphi}{\partial \sigma_2} \cdot \frac{\partial \sigma_2}{\partial \sigma_{ij}} + \frac{\partial \varphi}{\partial cos(2\theta)} \frac{\partial cos(2\theta)}{\partial \sigma_{ij}} \tag{13}$$

$$\frac{\partial \varphi}{\partial \sigma_{ij}} = \begin{Bmatrix} \frac{\partial \varphi}{\partial \sigma_{xx}} \\ \frac{\partial \varphi}{\partial \sigma_{yy}} \\ \frac{\partial \varphi}{\partial \sigma_{xy}} \end{Bmatrix} = \begin{bmatrix} \frac{\partial \sigma_1}{\partial \sigma_{xx}} & \frac{\partial \sigma_2}{\partial \sigma_{xx}} & \frac{\partial cos(2\theta)}{\partial \sigma_{xx}} \\ \frac{\partial \sigma_1}{\partial \sigma_{yy}} & \frac{\partial \sigma_2}{\partial \sigma_{yy}} & \frac{\partial cos(2\theta)}{\partial \sigma_{yy}} \\ \frac{\partial \sigma_1}{\partial \sigma_{xy}} & \frac{\partial \sigma_2}{\partial \sigma_{xy}} & \frac{\partial cos(2\theta)}{\partial \sigma_{xy}} \end{bmatrix} \cdot \begin{Bmatrix} \frac{\partial \varphi}{\partial \sigma_1} \\ \frac{\partial \varphi}{\partial \sigma_2} \\ \frac{\partial \varphi}{\partial cos(2\theta)} \end{Bmatrix} = [D] \cdot \begin{Bmatrix} \frac{\partial \varphi}{\partial \sigma_1} \\ \frac{\partial \varphi}{\partial \sigma_2} \\ \frac{\partial \varphi}{\partial cos(2\theta)} \end{Bmatrix} \tag{14}$$

$$[D] = \begin{bmatrix} \frac{1}{2}(1 + cos(2\theta)) & \frac{1}{2}(1 - cos(2\theta)) & \frac{sin^2(2\theta)}{\sigma_1 - \sigma_2} \\ \frac{1}{2}(1 - cos(2\theta)) & \frac{1}{2}(1 + cos(2\theta)) & -\frac{sin^2(2\theta)}{\sigma_1 - \sigma_2} \\ sin(2\theta) & -sin(2\theta) & -\frac{2sin(2\theta)cos(2\theta)}{\sigma_1 - \sigma_2} \end{bmatrix} \tag{15}$$

$$[D] = \begin{bmatrix} \frac{1}{2}(1 + c) & \frac{1}{2}(1 - c) & \frac{s^2}{\sigma_1 - \sigma_2} \\ \frac{1}{2}(1 - c) & \frac{1}{2}(1 + c) & -\frac{s^2}{\sigma_1 - \sigma_2} \\ s & -s & -\frac{2sc}{\sigma_1 - \sigma_2} \end{bmatrix} \tag{16}$$

where:

$s = sin\ (2\theta)$

$c = cos\ (2\theta)$

The independent variables in the above relations are the two principal stresses (σ_1 and σ_2) and angle θ between the material axes and directions of the principal stresses.

3.2. Kinematic Hardening Law

The Yoshida–Uemori model is based on the principle of two yield surfaces, where the inner surface behaves as a purely kinematic model (i.e., its shape does not change and only the origin of its coordinate system shifts due to the strain hardening). The second surface (outer one-bounding surface) behaves as a purely isotropic model (i.e., the origin of its coordinate system does not change and this surface is increasing due to the strain hardening). The outer yield surface (bounding surface) is thus the limiting factor for the displacement of the inner surface [51].

The chosen model allows us to properly describe all the phenomena occurring during the forming of thin sheets. These are mainly the so-called transient Bauschinger effect during the change of stress state and eventually the sharp yield point of the material. This model also allows expressing the change of Young's modulus depending on the plastic strain. As the most important input for proper setting of the required parameters defining the Yoshida–Uemori model, the true stress–strain curve (hardening curve) measured from the static tensile test and cyclic test as well was used. The change of the mechanical properties due to the Bauschinger effect can be seen in Figure 16.

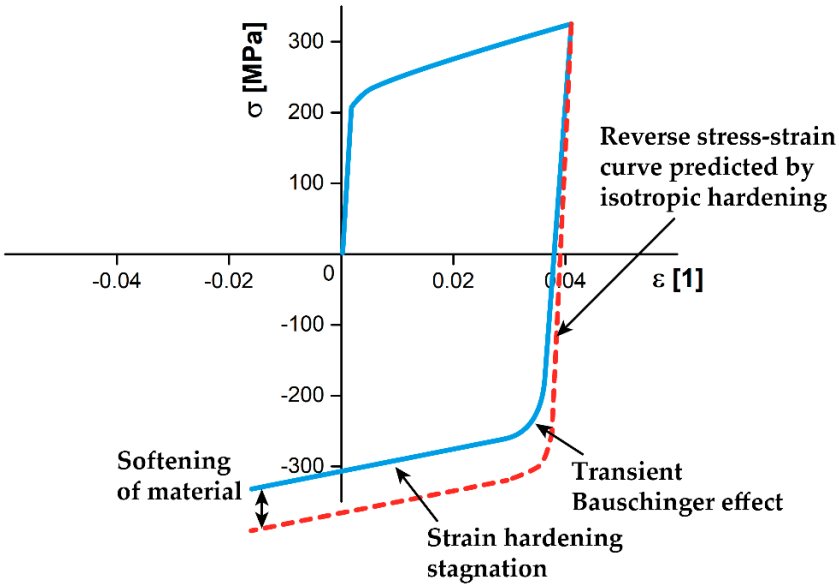

Figure 16. Change of mechanical properties due to the Bauschinger effect [51].

3.3. Definition of the Material Model in the Software PAM-STAMP 2G

Three material models were created in the software PAM-STAMP 2G for the numerical simulation of the bending process. In all cases, the Vegter anisotropic yield criterion based on the measured material characteristics from static tensile tests and HBT were used. Such yield criterion was subsequently combined with different types of hardening laws and the selection of surface or volume elements in the FEA. Finally, three combinations of the mathematical computational model were tested in this paper.

3.3.1. Vegter Yield Criterion in Combination with the Isotropic Hardening Law

Vegter anisotropic yield criterion as defined in the software PAM-STAMP 2G allows taking into account the yield strengths in the individual testing directions (in this case in directions 0°, 45° and 90° with respect to the rolling direction), the yield strength under the equi-biaxial loading (HBT) and plastic strain ratios (Lankford parameters) both from the static tensile test and HBT. In addition to these values, Young's modulus, Poisson's ratio and density of the material to be tested must be entered into the material card. In the case of isotropic hardening law, the stress–strain curve is defined as the average curve from the measured values in the individual tested directions. A weighted average of the relevant quantity (acc. to standard EN ISO 10 113/2020) is calculated from Equation (17). The material card with the Vegter yield criterion in combination with the isotropic hardening law can be seen in Figure 17. For the calculation, a surface element of the deformation mesh, thus "surface blank", was chosen.

$$x = \frac{1}{4}(x_0 + 2x_{45} + x_{90}) \quad (17)$$

where:

x—weighted average of the monitored quantity

x_0, x_{45}, x_{90}—measured values in the relevant directions

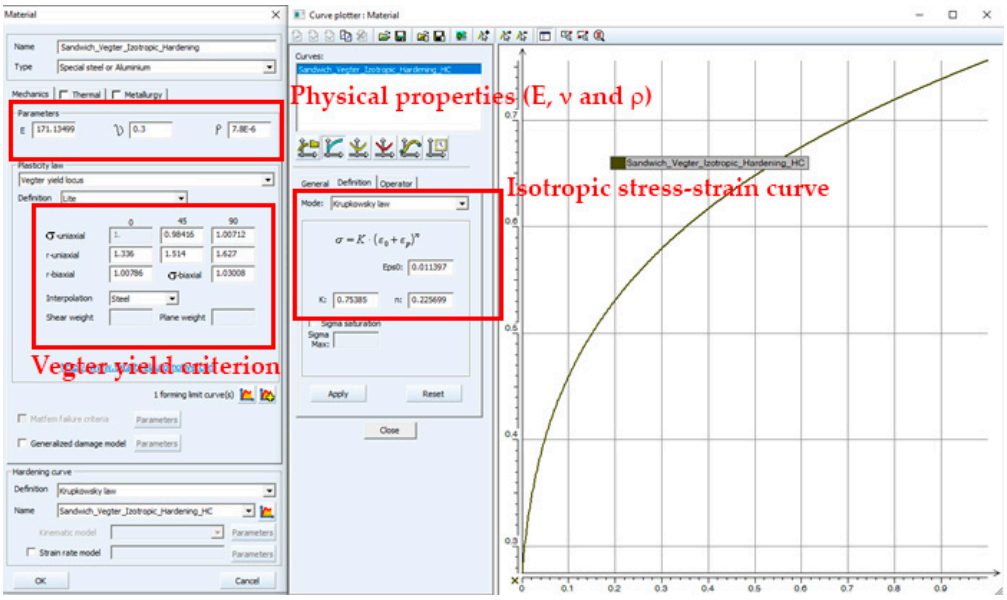

Figure 17. Material card (software PAM-STAMP 2G): Vegter yield criterion and isotropic hardening law.

3.3.2. Vegter Yield Criterion in Combination with the Kinematic Hardening Law

To determine the parameters for the model termed as the Yoshida–Uemori hardening law, it is necessary to calculate the parameters defining the kinematic hardening. For this purpose, the specialized software MatPara that has been developed and distributed by the authors of this model, was used. Input data for the calculation of the needed parameters are the data from tensile and cyclic tests. An example of fitting the measured curve to obtain material constants for the Yoshida–Uemori model can be seen in Figure 18. The material card for the Vegter yield criterion and kinematic hardening law is shown in Figure 19. For this material model, a surface element of mesh was chosen again.

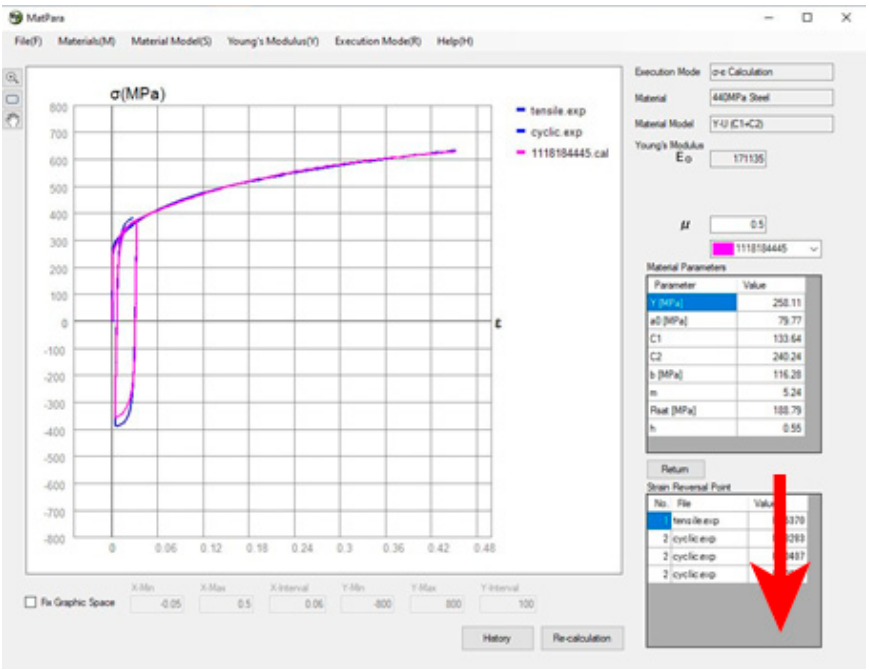

Figure 18. Software MatPara for calculation constants in the Yoshida–Uemori model.

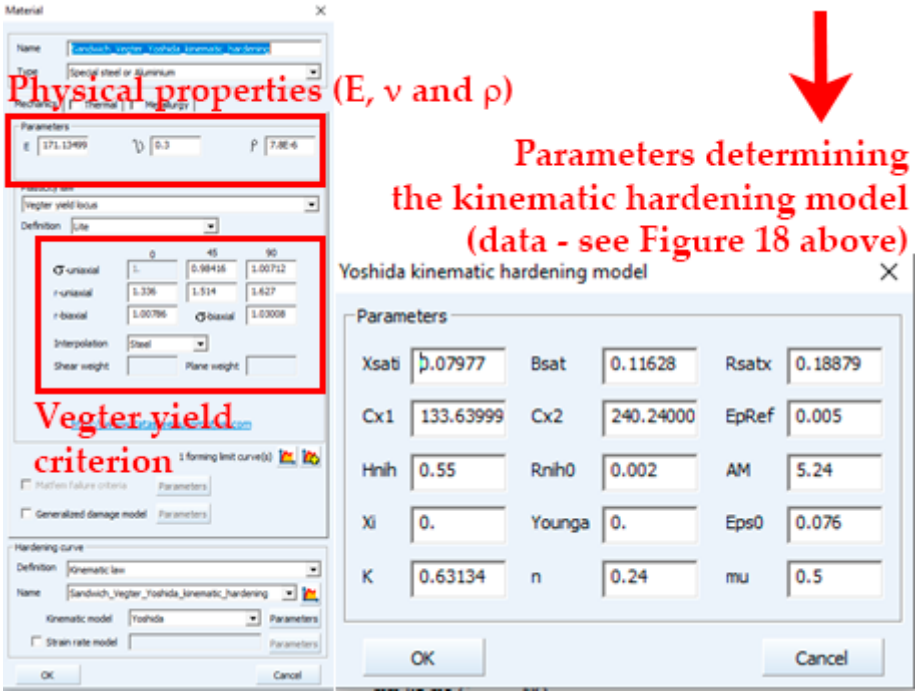

Figure 19. Material card: Vegter yield criterion and kinematic hardening law.

3.3.3. Vegter Yield Criterion in Combination with the Kinematic Hardening Law: Volume Element of the Deformation Mesh

Compared to the previous mathematical model, the volume element of the deformation mesh was chosen for this calculation. In the definition of the bend workpiece, a sheet is entered directly as a sandwich material and three layers are already taken into account for the calculation, as in the real process. Compared to the previous definition, the material definition must take into account the fact that the micro-alloyed steel layer itself has higher mechanical properties than the sandwich as a whole. In the previous cases, the sandwich was taken as a whole and (as is mentioned above) all measured values were related to the total sheet thickness. In this case, every layer was defined to directly correspond to its mechanical properties. In light of the micro-alloyed steel layer, there was only the need to recalculate the approximation constants to a smaller thickness (0.8 mm compared to the original 0.9 mm). The shape of the hardening curve did not change, the curve only shifts towards the higher values, which is reflected by an increase in the approximation constant K in Equation (1). On the other hand, it was quite difficult to determine the mechanical properties of the sandwich core. It was necessary to remove the layers of micro-alloyed steels and to test the mechanical properties of the thin central foil. From the measured values, the hardening curve was again constructed, see Figure 20.

When creating the model of the sheet for bending, the option "Volume Blank-sandwich" was selected in the PAM-STAMP 2G. This option allows (as was mentioned above) us to define the formed sheet by using existing volume elements with the possibility to define any number of layers and also any thickness of these layers. This is quite an advanced approach to specifying a sheet forming operation. However, when using volume elements, it is necessary to follow certain rules when selecting the suitable mesh parameters to keep the stability of the subsequent calculation. Dimensions of the volume element edges should not exceed a ratio of 1:4. Simultaneously, it is necessary to describe individual layers in the thickness direction. In this case, layers had thicknesses of 0.4–0.1–0.4 mm. The size of the element in the sheet thickness direction was thus more or less determined by the thinnest layer in the sandwich material. Furthermore, the minimal number of elements in the sheet thickness direction (which is usually five layers) must be observed. In this case, nine layers in the thickness direction and element having a size of 0.4 mm in the blank area

were chosen so that both the minimal number of elements and the aspect ratio of 1:4 were fulfilled. The own definition of a blank with volume elements can be seen in Figure 21.

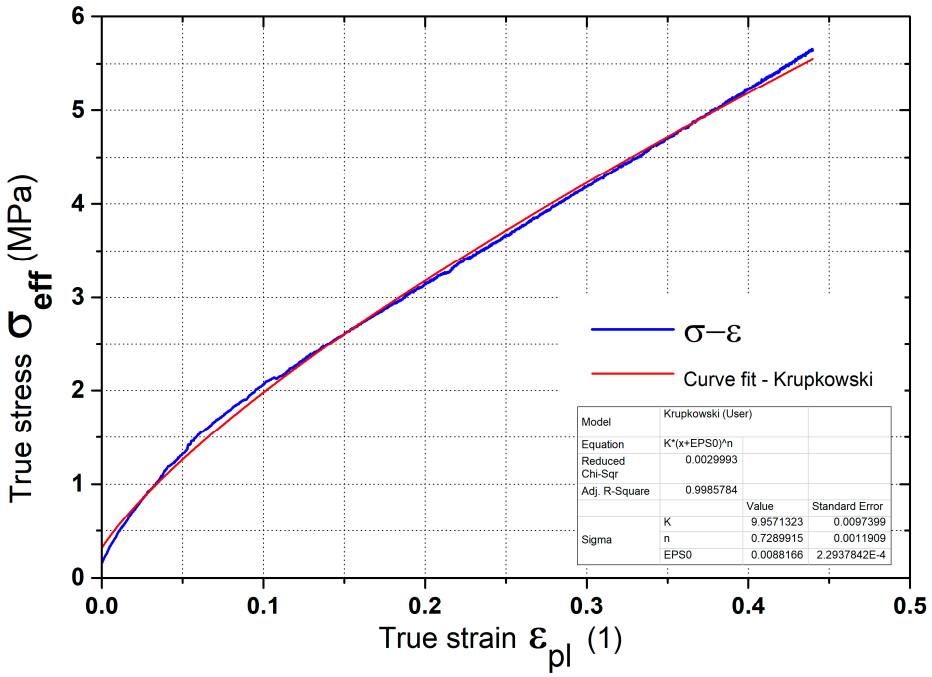

Figure 20. Stress–strain curve of the sandwich core from the acrylate copolymer.

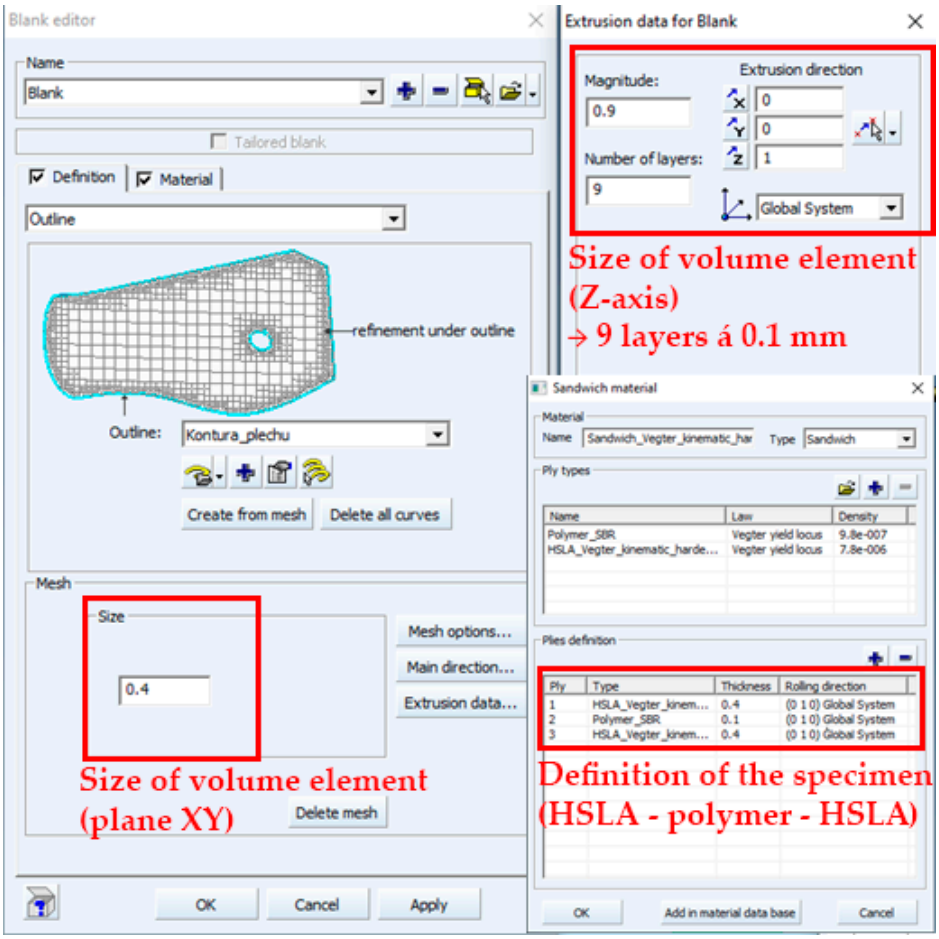

Figure 21. Definition of the blank using volume elements.

4. Results from the Finite Element Analysis (FEA)

Regarding the chosen material models, three calculations of the sheet metal forming process by bending technology were performed. In all cases, the same boundary conditions for the calculation were used (rigid tools, constant friction coefficient, constant bending punch feed rate, the position of the bottom dead centre, own course of the lower blank-holder force, etc.). For the evaluation of the numerical simulation accuracy, the criterion of matching the geometrical shape between the experimentally obtained shape and the shape obtained by the numerical simulations was chosen. When the springback computation was completed, the experimentally measured surface of the bent specimen was imported into the numerical simulation result and these two surfaces were subsequently compared. One of the post-processing options in the PAM-STAMP 2G is to express the dimensional deviations between two (or more) surfaces. This option was used, and the accuracy of the calculation was assessed based on this criterion. Due to the use of the volume element, the deviations were always related to the midplane of the sheet surfaces. Another possibility from the standard results evaluated in the sheet metal forming rested in the utilisation of the FLD diagram, which can be considered as a criterion for achieving the risk of rupture in the given part. For the chosen type of problem, any limit deformation was not achieved and the calculated deformations on the relevant bent part were well below the forming limit curve (FLC) for the tested sandwich material. The comparison of results between FEA and the real specimen can be seen in Figures 22–24.

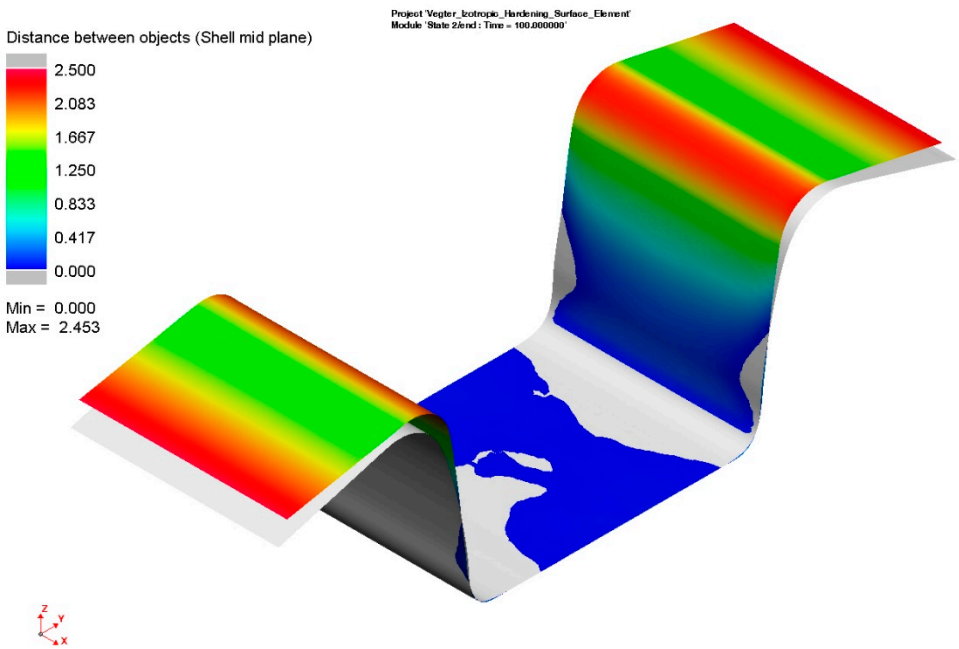

Figure 22. FEA: Vegter–isotropic hardening law–surface elements.

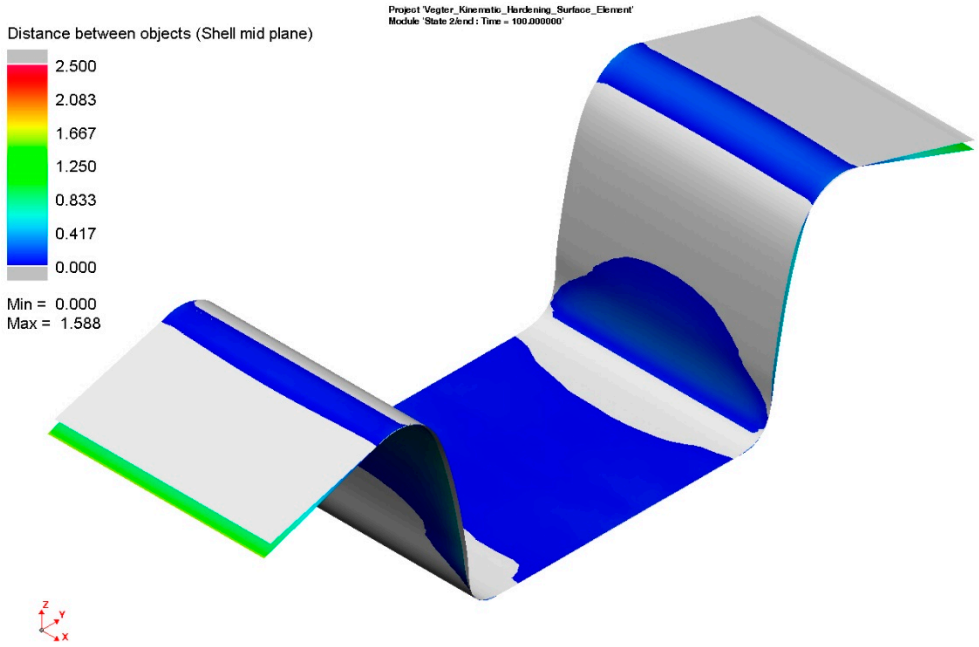

Figure 23. FEA: Vegter–kinematic hardening law–surface elements.

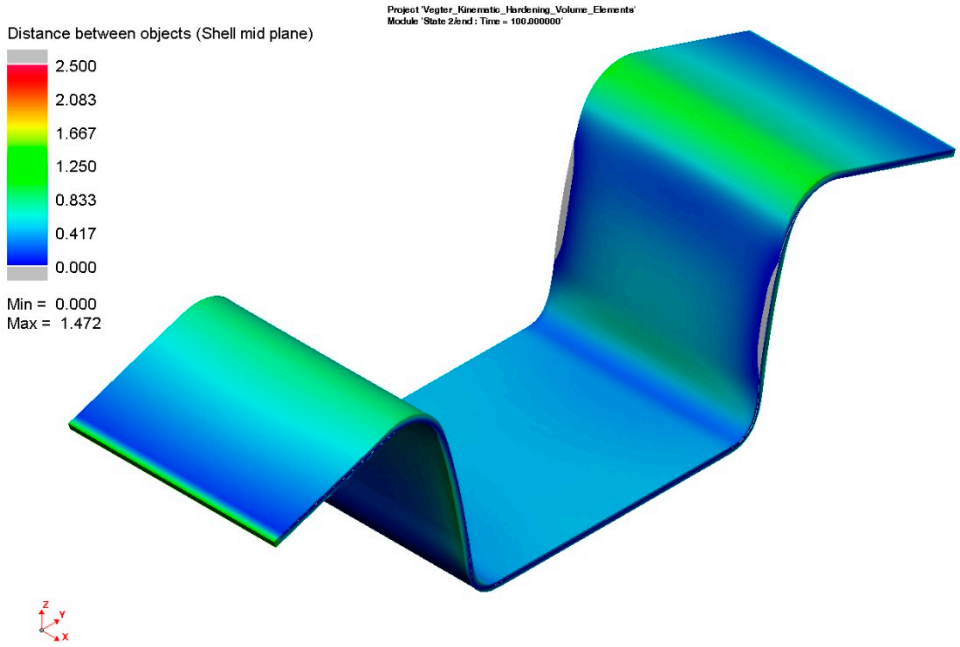

Figure 24. FEA: Vegter–kinematic hardening law–volume elements.

5. Discussion

Numerical simulations already represent a standard tool for predicting technological processes in industrial practice. In terms of practically achievable results, where high requirements are set on the accuracy and calculation speed, it is obvious that the proper choice of the mathematical model and the quality of input material data are some of the key factors influencing the final result of FEA. Previous studies have shown that the basic formability calculations can be performed just by using fundamental yield criterions in combination with a simple isotropic hardening law. The definitions of these models can be completed by performing the basic material tests; therefore, just using static tensile testing, where the time required to carry out these tests is relatively short. However, in cases where the technological operations involve the localisation of deformation (e.g.,

hemming) and there is also an increased requirement for predicting the final shape due to the springback effect, it is recommended to use the advanced computational models (e.g., Hill90, Barlat91, Barlat2000, Vegter or Yoshida 6th) in combination with a kinematic hardening law (e.g., Lemaitre and Chaboche or Yoshida–Uemori). The proper definition of these computational models means performing more time-consuming material tests. In addition to the standard static tensile test, there are tests performing under biaxial loading as well as shear, compression and cyclic tests. A frequently discussed issue is the selection of surface or volume elements of the computational mesh. From this point of view, for thin sheets up to a thickness of about 2 mm, it is generally recommended to use a surface element of the mesh. This approach significantly reduces the number of mesh elements, and the accuracy of calculation is considered to be sufficient compared to volume elements, where higher accuracy is assumed.

In this paper, the effect of the chosen calculation strategy on the FEA result was carried out. From the results presented in Figures 22–24, it is evident that the choice of the Vegter yield criterion in combination with the isotropic hardening law provides the worst results in light of the springback prediction. The maximum measured distance between the midplanes of the experimentally measured specimen and results obtained from the numerical simulation is about 2.5 mm (see Figure 22). To assess the deviations of the actual surface (experimentally obtained one) and the FEA surface, a longitudinal section was made along the axis of symmetry through both surfaces. Such a section can be seen in Figure 25, where all tested combinations with the experimentally measured shape (the real one), which is shown in blue colour, are compared. From the mutual comparison of these sections it can be seen that there is a fairly good matching in the bending punch radii (lower parts of the bending punch). However, the results of sections on the bending die drawing edge (upper parts of the specimen) already revealed considerable variations at the use of isotropic hardening law.

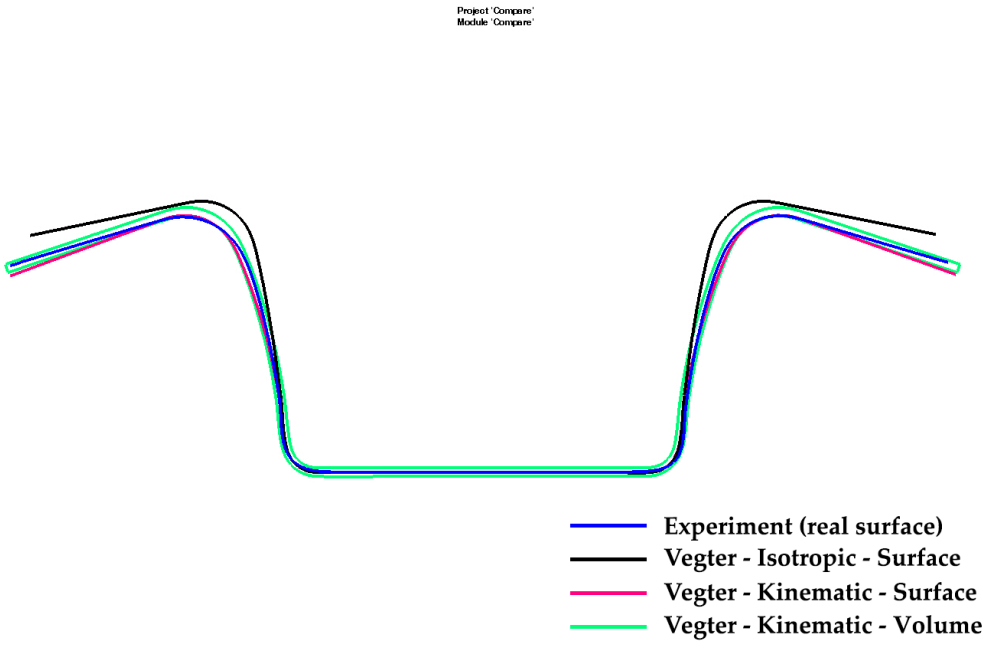

Figure 25. Final comparison along the section for results from FEA and experiments.

As in the previous case, a section through the resulting surfaces (see Figure 23) was performed when the Vegter yield criterion in combination with the kinematic law and surface elements was chosen. The final sections can be seen also in Figure 25. These results show quite a good shape matching both in the lower parts of the bending punch and in the upper parts of the specimen at bending on the drawing edge of the bending die. The maximum measured deviation between the midplanes in this case was 1.59 mm. It is quite important that this deviation occurs only in the peripheral parts of the specimen and is

largely influenced by the flange length. For the proper assessment of the shape matching, the most important from a practical point of view is the shape matching in the areas of rounding (radii area) and the walls between these radii. From Figures 22–24 can be seen that minimal differences could be found in these zones (order of 0.1 mm).

The last evaluated computational model combined the Vegter yield criterion with kinematic hardening law and volume elements. The FEA result was assessed again based upon Figure 24 and also on the performed section, which can be seen in the green colour again in Figure 25. In addition, in this case, the red colour is the shape of the experimentally obtained specimen and the grey colour is from the FEA. The results again show a very good shape matching both in the lower parts of the bending punch (radii) as well as in the upper parts of the specimen on the drawing edge of the bending die. The maximum measured deviation between the midplanes in this case was 1.47 mm, and in light of the shape, similar conclusions can be made as in the previous case where surface elements were used.

In light of the quantitative comparison of achieved results, histograms of deviations between experimentally and numerically determined surfaces were used. In the following Figures 26–28, these histograms are shown (deviations between surfaces vs. relevant frequency) for all tested combinations. Concerning the obtained results and their comprehensible display, results were divided into five deviation regions with a step size of 0.5 mm (thus 0–0.5–1–1.5–2–2.5 mm).

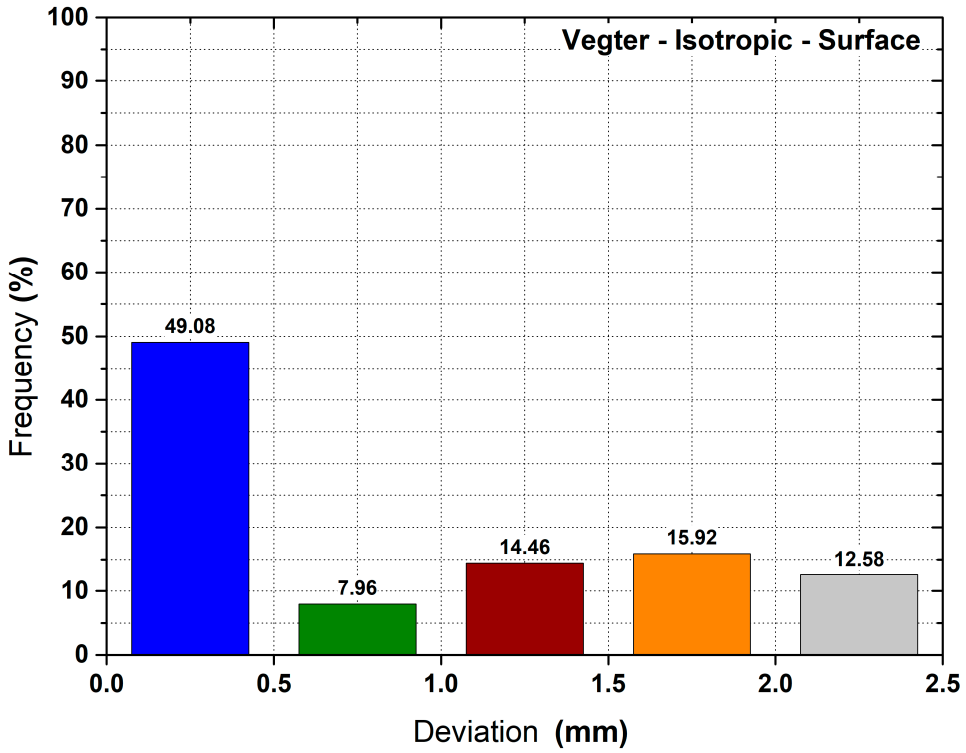

Figure 26. Distribution of deviations between determined surfaces: Vegter–isotropic hardening law–surface elements.

Figure 26 shows the distribution of deviations between real and computed surfaces by using the Vegter yield criterion, isotropic hardening law and surface elements.

The distribution of deviations between real and computed surfaces by using Vegter yield criterion, kinematic hardening law and surface elements is given in Figure 27.

Finally, Figure 28 illustrates almost the same situation as in the previous case; however, volume elements of the deformation mesh are used in this case.

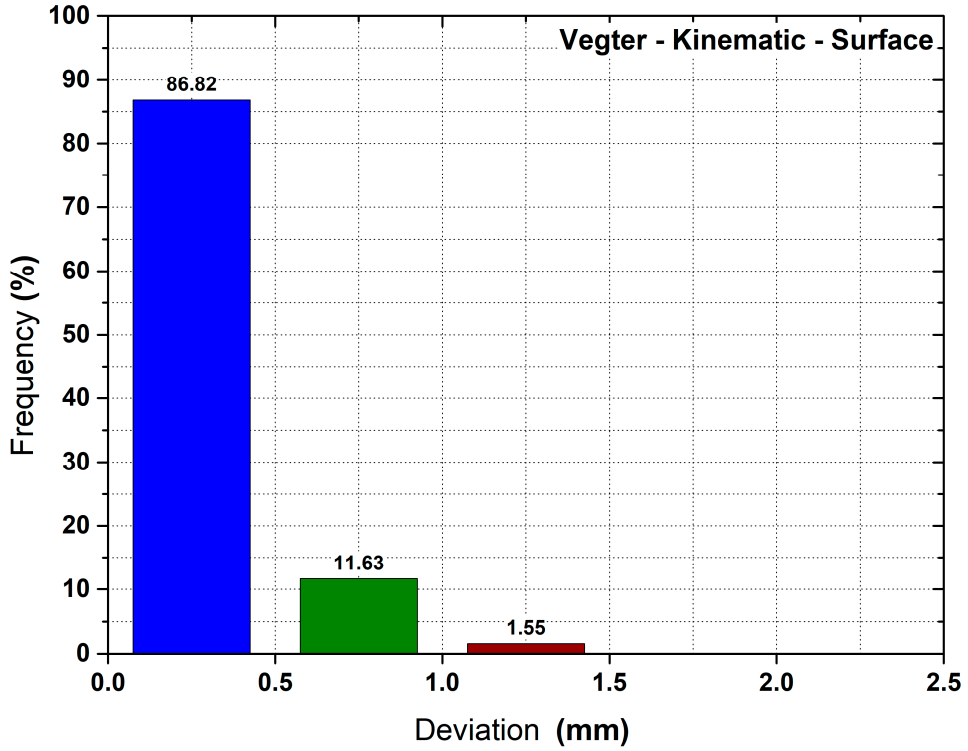

Figure 27. Distribution of deviations between determined surfaces: Vegter–kinematic hardening law–surface elements.

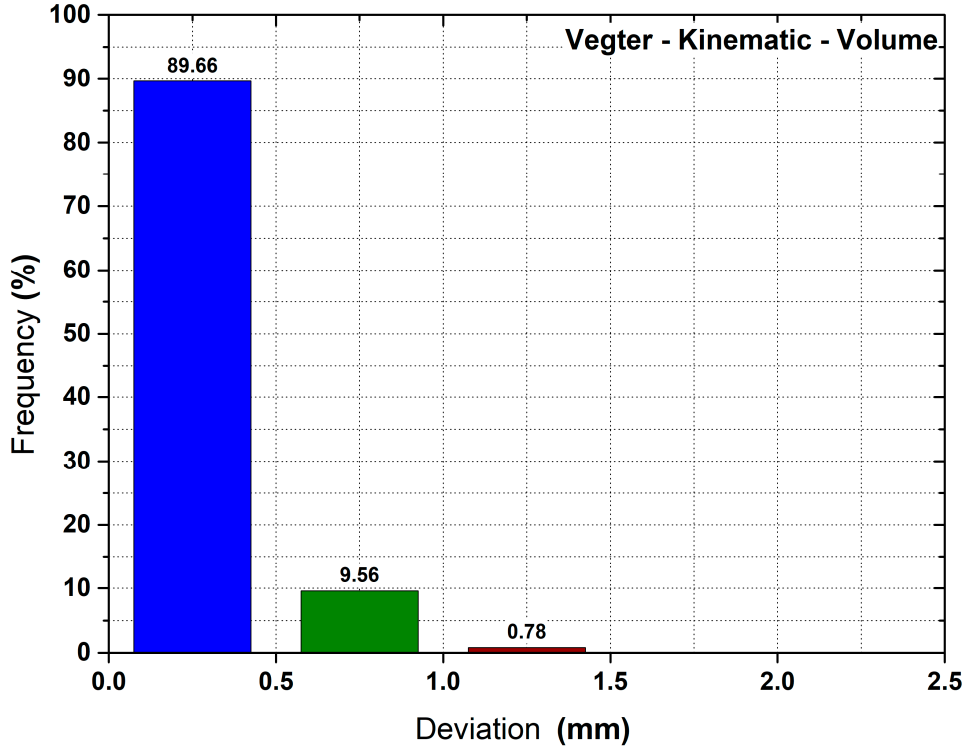

Figure 28. Distribution of deviations between determined surfaces: Vegter–kinematic hardening law–volume elements.

From the previous figures it is obvious that in light of the deviations between real and computed surfaces, the utilisation of the isotropic hardening law provides by far the worst results from all tested combinations. Only about 50% of such deviations could be found up

to 0.5 mm. In addition to that, quite a high frequency of 12.58% was determined for the maximal range of deviations (2–2.5 mm). On the other hand, results from the kinematic hardening laws revealed maximal values up to 1.5 mm. More precisely, the maximal deviation was 1.588 mm for surface elements (see Figure 23), but its proportion was zero due to rounding. Moreover, the vast majority (about 90%) of these values could be found in the first range of deviations (0–0.5 mm). Slightly better results were determined by using the volume elements.

When an isotropic hardening law is chosen, it is evident that this model is not able to describe accurately enough the change in the stress state on the drawing edge, which significantly affects the stress and strain in the formed material and thus also the subsequent springback of the used material. From the results, it can be seen that in the lower parts of the specimen on the bending punch radii, where any change of stress state does not occur, the accuracy is quite sufficient for all chosen material models. In the upper parts on the bending die drawing edge, where a change of the stress state already occurs, the FEA results are greatly influenced by the choice of the calculation model. The kinematic hardening law provides significantly more accurate results than the isotropic hardening law. When comparing the FEA results, which use the same computational model (Vegter yield criterion and kinematic hardening law), but differ in the used meshing strategy (surface element vs. volume element), it can be seen that both models provide very similar results. Both used models show quite a high shape matching with the experimentally measured ones. The model with surface elements slightly underestimates the springback magnitude, while the model with volume elements slightly overestimates the springback magnitude compared to the experiment results. However, these differences are minimal, and the calculation accuracy can be considered satisfactory in both cases. On the other hand, the choice of a volume element in the case of sheets having lower thicknesses significantly increases the total number of elements used in the computational mesh. The model with surface elements had 4200 elements (square elements selected with the edge of 1 mm) compared to 236, 250 volume elements. Such a significant increase in the number of elements leads to a hundred-fold increase in the computational time (minutes for surface elements vs. hours for volume elements).

6. Conclusions

The major aim of the research presented in this paper was to determine the influence of the computational material model (generally meshing strategy) on the result of the FEA springback prediction for a sandwich material made from a micro-alloyed steel and acrylate copolymer. Different material models describing the deformation behaviour of the tested sandwich material in the plastic state (isotropic hardening law vs. kinematic hardening law) were tested in the experimental part. Furthermore, the effect of the selection of the dimensional type of mesh element (surface element vs. volume element) on the result of the numerical simulation were investigated as well. The following conclusions can be stated from the measured and computed results:

1. The isotropic hardening law cannot be used to correctly predict the springback of sandwich material in cases where the stress state changes during the forming process.
2. The kinematic hardening law provides a more accurate springback prediction compared to the isotropic hardening model regardless of the surface or volume element selection for the computational mesh.
3. The choice of the meshing strategy does not have any significant effect on the FEA result when the kinematic hardening law is used. The surface and volume elements give almost exactly comparable results for the springback prediction of the sandwich material.
4. From a quantitative point of view (using histograms of surfaces' deviations, see Figures 26–28), it was confirmed that the kinematic hardening law (regardless of the element type) has significantly higher accuracy in springback prediction than the isotropic hardening law. In addition to that, both kinematic hardening laws (surface

and volume type of mesh) have almost 90% of the surfaces' deviations up to 0.5 mm compared to the isotropic hardening law, where only 46% can be found up to 0.5 mm.
5. The definition of the sandwich material using layers of volume elements in the deformation mesh does not provide a significant improvement of the FEM result.
6. In the numerical simulation of forming the sandwich material, the measured values of the mechanical quantities can be related to the entire sheet (sandwich) thickness, and it is not necessary to distinguish the different deformation and stress behaviour of the individual layers.
7. From the calculation accuracy point of view, it does not make any sense to use volume elements of the deformation mesh for the thin sheets. Such an approach leads only to a significant increase in computational time.

Author Contributions: Conceptualisation, P.S. and J.S.; methodology, P.S.; investigation, J.S. and D.K.; resources, P.S. and J.S.; data curation, P.S. and J.S.; writing—original draft preparation, P.S.; writing—review and editing, P.S. and J.S.; visualisation, P.S. and J.S.; supervision, P.S.; funding acquisition, J.S. All authors have read and agreed to the published version of the manuscript.

Funding: This research received no external funding.

Institutional Review Board Statement: Not applicable.

Informed Consent Statement: Not applicable.

Data Availability Statement: Not applicable.

Conflicts of Interest: The authors declare no conflict of interest.

References

1. Fischer, S. Aluminium foldcores for sandwich structure application: Mechanical properties and FE-simulation. *Thin Walled Struct.* **2015**, *90*, 31–41. [CrossRef]
2. Grygorowicz, M.; Magnucki, K.; Malinowski, M. Elastic buckling of a sandwich beam with variable mechanical properties of the core. *Thin Walled Struct.* **2015**, *87*, 127–132. [CrossRef]
3. Sivaram, A.R.; Manikandan, N.; Krishnakumar, S.K.; Rajavel, R.; Krishnamohan, S.; Vijayaganth, G. Experimental study on aluminium based sandwich composite with polypropylene foam sheet. *Mater. Today Proc.* **2020**, *24*, 746–753. [CrossRef]
4. Arbaoui, J.; Schmitt, Y.; Pierrot, J.-L.; Royer, F.-X. Numerical simulation and experimental bending behaviour of multi-layer sandwich structures. *J. Theor. Appl. Mech.* **2014**, *52*, 431–442.
5. Li, X.; Lin, Y.; Lu, F. Numerical simulation on in-plane deformation characteristics of lightweight aluminum honeycomb under direct and indirect explosion. *Materials* **2019**, *12*, 2222. [CrossRef] [PubMed]
6. Wang, Z.; Li, Z.; Xiong, W. Numerical study on three-point bending behavior of honeycomb sandwich with ceramic tile. *Compos. Part B Eng.* **2019**, *167*, 63–70. [CrossRef]
7. Xie, S.; Feng, Z.; Zhou, H.; Wang, D. Three-point bending behavior of nomex honeycomb sandwich panels: Experiment and simulation. *Mech. Adv. Mater. Struct.* **2021**, *28*, 1917–1931. [CrossRef]
8. Bi, G.; Yin, J.; Wang, Z.; Jia, Z. Micro fracture behavior of composite honeycomb sandwich structure. *Materials* **2021**, *14*, 135. [CrossRef]
9. Gao, X.; Zhang, M.; Huang, Y.; Sang, L.; Hou, W. Experimental and numerical investigation of thermoplastic honeycomb sandwich structures under bending loading. *Thin Walled Struct.* **2020**, *155*, 106961. [CrossRef]
10. Wu, X.; Yu, H.; Guo, L.; Zhang, L.; Sun, X.; Chai, Z. Experimental and numerical investigation of static and fatigue behaviors of composites honeycomb sandwich structure. *Compos. Struct.* **2019**, *213*, 165–172. [CrossRef]
11. Yu, G.-C.; Feng, L.-J.; Wu, L.-Z. Thermal and mechanical properties of a multifunctional composite square honeycomb sandwich structure. *Mater. Des.* **2016**, *102*, 238–246. [CrossRef]
12. Liu, J.; Wang, Z.; Hui, D. Blast resistance and parametric study of sandwich structure consisting of honeycomb core filled with circular metallic tubes. *Compos. Part B Eng.* **2018**, *145*, 261–269. [CrossRef]
13. Gladkovsky, S.V.; Kuteneva, S.V.; Sergeev, S.N. Microstructure and mechanical properties of sandwich copper/steel composites produced by explosive welding. *Mater. Charact.* **2019**, *154*, 294–303. [CrossRef]
14. Nilsson, P.; Al-Emrani, M.; Atashipour, S.R. Fatigue-strength assessment of laser welds in corrugated core steel sandwich panels. *J. Constr. Steel Res.* **2020**, *164*, 105797. [CrossRef]
15. Nilsson, P.; Hedegård, J.; Al-Emrani, M.; Atashipour, S.R. The impact of production-dependent geometric properties on fatigue-relevant stresses in laser-welded corrugated core steel sandwich panels. *Weld World* **2019**, *63*, 1801–1818. [CrossRef]
16. Lee, H.S.; Yoon, J.H.; Yoo, J.T. Application of solid state joining technologies in aerospace parts. *Key Eng. Mater.* **2020**, *837*, 69–73. [CrossRef]

17. Pragana, J.P.; Contreiras, T.R.; Bragança, I.M.; Silva, C.M.; Alves, L.M.; Martins, P.A. Joining by forming of metal–polymer sandwich composite panels. *Proc. Inst. Mech. Eng. Part B J. Eng. Manuf.* **2019**, *233*, 2089–2098. [CrossRef]
18. Ablat, M.A.; Qattawi, A. Numerical simulation of sheet metal forming: A review. *Int. J. Adv. Manuf. Technol.* **2017**, *89*, 1235–1250. [CrossRef]
19. Zajkani, A.; Hajbarati, H. An analytical modeling for springback prediction during U-bending process of advanced high-strength steels based on anisotropic nonlinear kinematic hardening model. *Int. J. Adv. Manuf. Technol.* **2017**, *90*, 349–359. [CrossRef]
20. Li, Y.; Liang, Z.; Zhang, Z.; Zou, T.; Li, D.; Ding, S.; Xiao, H.; Shi, L. An analytical model for rapid prediction and compensation of springback for chain-die forming of an AHSS U-channel. *Int. J. Mech. Sci.* **2019**, *159*, 195–212. [CrossRef]
21. Hajbarati, H.; Zajkani, A. A novel analytical model to predict springback of DP780 steel based on modified Yoshida-Uemori two-surface hardening model. *Int. J. Mater.* **2019**, *12*, 441–455. [CrossRef]
22. Yang, X.; Choi, C.; Sever, N.K.; Altan, T. Prediction of springback in air-bending of advanced high strength steel (DP780) considering Young's modulus variation and with a piecewise hardening function. *Int. J. Mech. Sci.* **2016**, *105*, 266–272. [CrossRef]
23. Liu, J.; Xue, W. Unconstrained bending and springback behaviors of aluminum-polymer sandwich sheets. *Int. J. Adv. Manuf. Technol.* **2017**, *91*, 1517–1529. [CrossRef]
24. Gautam, V.; Raut, V.M.; Kumar, D.R. Analytical prediction of springback in bending of tailor-welded blanks incorporating effect of anisotropy and weld zone properties. *Proc. Inst. Mech. Eng. Part L J. Mater. Des. Appl.* **2018**, *232*, 294–306. [CrossRef]
25. Zhang, Z.K.; Wu, J.J.; Guo, R.C.; Wang, M.Z.; Li, F.F.; Guo, S.C.; Wang, Y.A.; Liu, W.P. A semi-analytical method for the springback prediction of thick-walled 3D tubes. *Mater. Des.* **2016**, *99*, 57–67. [CrossRef]
26. Jin, L.; Yang, Y.-F.; Li, R.-Z.; Cui, Y.-W.; Jamil, M.; Li, L. study on springback straightening after bending of the U-section of TC4 material under high-temperature conditions. *Materials* **2020**, *13*, 1895. [CrossRef]
27. Wasif, M.; Iqbal, S.A.; Tufail, M.; Karim, H. Experimental analysis and prediction of springback in V-bending process of high-tensile strength steels. *Trans. Indian Inst. Met.* **2020**, *73*, 285–300. [CrossRef]
28. Panthi, S.K.; Ramakrishnan, N. Semi analytical modeling of springback in arc bending and effect of forming load. *Trans. Nonferrous Met. Soc. China* **2011**, *21*, 2276–2284. [CrossRef]
29. Han, Y.S.; Yang, W.H.; Choi, K.Y.; Kim, B.H. A Study on the effect of input parameters on springback prediction accuracy. In *AIP Conference Proceedings*; American Institute of Physics: College Park, MD, USA, 2011; Volume 1383, pp. 1137–1142. [CrossRef]
30. Mertin, C.; Stellmacher, T.; Schmitz, R.; Hirt, G. Enhanced springback prediction for bending of high-strength spring steel using material data from an inverse modelling approach. *Procedia Manuf.* **2019**, *29*, 153–160. [CrossRef]
31. Gu, B.; He, J.; Li, S.; Chen, Y.; Li, Y. Cyclic sheet metal test comparison and parameter calibration for springback prediction of dual-phase steel sheets. *J. Manuf. Sci. Eng.* **2017**, *139*, 91010. [CrossRef]
32. Li, Y.; Li, A.; Yue, Z.; Qiu, L.; Badreddine, H.; Gao, J.; Wang, Y. Springback prediction of AL6061 pipe in free bending process based on finite element and analytic methods. *Int. J. Adv. Manuf. Technol.* **2020**, *109*, 1789–1799. [CrossRef]
33. Seo, K.-Y.; Kim, J.-H.; Lee, H.-S.; Kim, J.H.; Kim, B.-M. Effect of constitutive equations on springback prediction accuracy in the TRIP1180 cold stamping. *Metals* **2018**, *8*, 18. [CrossRef]
34. Liu, X.; Cao, J.; Chai, X.; Liu, J.; Zhao, R.; Kong, N. Investigation of forming parameters on springback for ultra high strength steel considering Young's modulus variation in cold roll forming. *J. Manuf. Process.* **2017**, *29*, 289–297. [CrossRef]
35. Pouraliakbar, H.; Khalaj, G.; Jandaghi, M.R.; Khalaj, M.J. Study on the correlation of toughness with chemical composition and tensile test results in microalloyed API pipeline steels. *J. Min. Metall. B Metall.* **2015**, *51*, 173–178. [CrossRef]
36. Jamli, M.R.; Farid, N.M. The sustainability of neural network applications within finite element analysis in sheet metal forming: A review. *Measurement* **2019**, *138*, 446–460. [CrossRef]
37. Angsuseranee, N.; Pluphrach, G.; Watcharasresomroeng, B.; Songkroh, A. Springback and sidewall curl prediction in U-bending process of AHSS through finite element method and artificial neural network approach. *Songklanakarin J. Sci. Technol.* **2018**, *40*, 534–539.
38. Miranda, S.S.; Barbosa, M.R.; Santos, A.D.; Pacheco, J.B.; Amaral, R.L. Forming and springback prediction in press brake air bending combining finite element analysis and neural networks. *J. Strain Anal. Eng. Des.* **2018**, *53*, 584–601. [CrossRef]
39. Zhu, Y.X.; Liu, Y.L.; Yang, H.; Li, H.P. Development and application of the material constitutive model in springback prediction of cold-bending. *Mater. Des.* **2012**, *42*, 245–258. [CrossRef]
40. Chatti, S.; Fathallah, R. A study of the variations in elastic modulus and its effect on springback prediction. *Int. J. Mater.* **2014**, *7*, 19–29. [CrossRef]
41. Jung, J.; Jun, S.; Lee, H.-S.; Kim, B.-M.; Lee, M.-G.; Kim, J.H. Anisotropic hardening behaviour and springback of advanced high-Strength steels. *Metals* **2017**, *7*, 480. [CrossRef]
42. Baara, W.A.B.; Baharudin, B.T.H.T.B.; Anuar, M.K.; Ismail, M.I.S. Effect of elastic module degradation measurement in different sizes of the nonlinear isotropic–kinematic yield surface on springback prediction. *Metals* **2019**, *9*, 511. [CrossRef]
43. Mulidrán, P.; Spišák, E.; Tomáš, M.; Slota, J.; Majerníková, J. Numerical prediction and reduction of hat-shaped part springback made of dual-phase AHSS steel. *Metals* **2020**, *10*, 1119. [CrossRef]
44. Mulidrán, P.; Šiser, M.; Slota, J.; Spišák, E.; Sleziak, T. Numerical prediction of forming car body parts with emphasis on springback. *Metals* **2018**, *8*, 435. [CrossRef]
45. Trzepiecinski, T.; Lemu, H.G. Effect of computational parameters on springback prediction by numerical simulation. *Metals* **2017**, *7*, 380. [CrossRef]

46. Naofal, J.; Naeini, H.M.; Mazdak, S. Effects of hardening model and variation of elastic modulus on springback prediction in roll forming. *Metals* **2019**, *9*, 1005. [CrossRef]
47. Sumikawa, S.; Ishiwatari, A.; Hiramoto, J.; Urabe, T. Improvement of springback prediction accuracy using material model considering elastoplastic anisotropy and Bauschinger effect. *J. Mater. Process. Technol.* **2016**, *230*, 1–7. [CrossRef]
48. Slota, J.; Šiser, M.; Dvorák, M. Experimental and numerical analysis of springback behavior of aluminum alloys. *Strength Mater.* **2017**, *49*, 565–574. [CrossRef]
49. Vegter, H.; van den Boogaard, A.H. A plane stress yield function for anisotropic sheet material by interpolation of biaxial stress states. *Int. J. Plast.* **2006**, *22*, 557–580. [CrossRef]
50. ESI Group. *Pam-Stamp 2020.5 User's Guide*; ESI Group: Paris, France, 2020.
51. Yoshida, F.; Uemori, T. A model of large-strain cyclic plasticity and its application to springback simulation. *Int. J. Mech. Sci.* **2003**, *45*, 1687–1702. [CrossRef]